Science

AAAS

The Amount of Recycled Crust in Sources of Mantle-Derived Melts

Alexander V. Sobolev,[1,2]* Albrecht W. Hofmann,[1] Dmitry V. Kuzmin,[1,3] Gregory M. Yaxley,[4] Nicholas T. Arndt,[5] Sun-Lin Chung,[6] Leonid V. Danyushevsky,[7] Tim Elliott,[8] Frederick A. Frey,[9] Michael O. Garcia,[10] Andrey A. Gurenko,[1] Vadim S. Kamenetsky,[7] Andrew C. Kerr,[11] Nadezhda A. Krivolutskaya,[2] Vladimir V. Matvienkov,[12] Igor K. Nikogosian,[13,14] Alexander Rocholl,[15] Ingvar A. Sigurdsson,[16] Nadezhda M. Sushchevskaya,[2] Mengist Teklay[17]

Plate tectonic processes introduce basaltic crust (as eclogite) into the peridotitic mantle. The proportions of these two sources in mantle melts are poorly understood. Silica-rich melts formed from eclogite react with peridotite, converting it to olivine-free pyroxenite. Partial melts of this hybrid pyroxenite are higher in nickel and silicon but poorer in manganese, calcium, and magnesium than melts of peridotite. Olivine phenocrysts' compositions record these differences and were used to quantify the contributions of pyroxenite-derived melts in mid-ocean ridge basalts (10 to 30%), ocean island and continental basalts (many >60%), and komatiites (20 to 30%). These results imply involvement of 2 to 20% (up to 28%) of recycled crust in mantle melting.

I t is widely accepted that the heterogeneity of the convecting mantle observed in the composition of mantle-derived magmas is largely due to subduction and recycling of oceanic crust into the deep mantle (1, 2). To understand the role of crustal material in creating compositional heterogeneities in the mantle and to evaluate the geodynamical consequences of this contribution, one must quantify the crustal input to the mantle sources of common, mantle-derived magmas in mid-oceanic ridges basalts (MORBs), ocean islands (OIBs), and large igneous provinces (LIPs). It is not possible to use incompatible element abundances in basalts to constrain the proportion of recycled component in the magma source because concentrations of these elements are also sensitive to the extent of melting. Similarly, the use of isotope ratios for making such quantitative estimates is compromised by the isotopic variability of subducted materials involved in the recycling process (2). We used an alternative approach based on a combination of major elements and compatible trace elements in parental melts, because these are more uniform in the mantle and are strongly controlled by the residual phases in equilibrium with partial melts (3–5).

Our method has its basis in the experimental and theoretical prediction that high-pressure (P > 3.0 GPa) melting of typical recycled oceanic crust (in the form of eclogite with a separate SiO_2 phase) and reaction of this melt with peridotite produces olivine-free pyroxenite (5). We show that further melting of this hybrid lithology in the absence of residual olivine is more voluminous than the melting of peridotite (at a given pressure and temperature) and that pyroxenite-derived melts are characteristically enriched in Si and Ni but depleted in Mg, Ca, and Mn compared with their peridotite-derived counterparts. This difference arises because olivine principally controls the composition of melt produced in peridotite, whereas pyroxene mainly controls the composition of melt from olivine-free hybrid pyroxenite (5–8). Experimental data predict (9) that, as such pyroxenite-derived melts rise toward the surface, the decrease in pressure causes their saturation in olivine. This olivine is unusually Ni rich and Mn and Ca poor. With use of a new, large data set of high-precision analyses of olivine phenocrysts from OIBs, LIPs, MORBs, and komatiites, we show that hybrid pyroxenite is a common lithology in upwelling mantle and a major contributor to tholeiitic (silica-saturated) and transitional (moderately silica-undersaturated) magmas of OIBs and LIPs emplaced on thick oceanic or continental lithosphere.

Olivine data set. We use olivine phenocrysts as probes of parental melt composition, because olivine is the first phase to precipitate at low pressures in almost all mantle-derived magmas and because its forsterite content is an excellent measure of the degree of fractional crystallization allowing reconstruction of the parental melt composition.

Olivine phenocrysts were analyzed by electron microprobe using high probe currents and long counting times (10). This procedure routinely yields detection limits of around 6 to 15 parts per million (ppm) and errors (2 standard errors) of 15 to 30 ppm for trace elements (Ni, Ca, Mn, Cr, Co, and Al) and 0.01 mole percent (mol %) for forsterite content [defined as Fo = Mg/(Mg + Fe)], checked by repeated analysis of San Carlos olivine standard (11). In the following diagrams we use only high-precision data.

We have analyzed nearly 17,000 grains of olivine phenocrysts from 229 samples of tholeiitic to transitional compositions covering MORBs (40 samples) from Mid-Atlantic Ridge, East Pacific Rise, South-East Indian Ridge, and Knipovich Ridge; OIBs (138 samples) from Hawaiian Islands and Emperor Seamounts, Canary Islands, Reunion, Azores, and Iceland; LIPs (36 samples) from Ontong Java Plateau, Siberia, Emeishan, Karoo, Afar, and North Atlantic Province; komatiites and associated picrites (15 samples) from the Archean Abitibi greenstone belt in Canada and the Belingwe belt in Zimbabwe and South Africa; Proterozoic komatiitic basalts from Gilmour Island, Canada; and komatiites and picrites from Gorgona Island, Colombia. Most samples are picrites or olivine basalts containing large amounts of fresh, high-magnesium olivine phenocrysts. The samples are subdivided into four groups: (i) MORB; (ii) within plate magmas (WPM, magmas erupted far from plate boundaries) forming OIB emplaced over thin lithosphere (<70 km thick), WPM-THIN; (iii) WPM (OIB and LIP) emplaced over thick lithosphere (>70 km thick), WPM-THICK; and (iv) komatiites and associated magmas, KOMATIITES. Details of sample locations, references for sample descriptions, and their group correspondence are presented in table S2a.

The most-magnesian olivine compositions (defined by olivines phenocrysts with Fo within 1 mol % from a maximum Fo) for each specimen were averaged (table S2a) for the plots shown in Fig. 1. Individual olivine analyses are presented on fig. S4 and tables S2, c to f.

In addition to Mn and Ni concentrations, which strongly correlate with Fo (Fig. 1, A and

[1]Max Planck Institute (MPI) for Chemistry, Post Office Box 3060, 55020 Mainz, Germany. [2]Vernadsky Institute of Geochemistry and Analytical Chemistry, Russian Academy of Sciences, Kosygin Street 19, 119991 Moscow, Russia. [3]Institute of Geology and Mineralogy, Siberian Branch of Russian Academy of Sciences, Koptuyga prospekt 3, 630090 Novosibirsk, Russia. [4]Research School of Earth Sciences, Australian National University, Canberra, ACT 0200 Australia. [5]Laboratoire de Géodynamique des Chaînes Alpines, Université de Grenoble, 38401 Grenoble cedex, France. [6]Department of Geosciences, National Taiwan University, Post Office Box 13-318, Taipei 106, Taiwan. [7]Australian Research Council, Centre of Excellence in Ore Deposits and School of Earth Sciences, University of Tasmania, Private Bag 79, Hobart, Tasmania, 7001, Australia. [8]Department of Earth Sciences, Queen's Road, Wills Memorial Building, University of Bristol, Bristol BS8 1RJ, UK. [9]Department of Earth, Atmospheric and Planetary Science, Massachusetts Institute of Technology (MIT), 77 Massachusetts Avenue, Cambridge, MA 02139, USA. [10]Department of Geology and Geophysics, University of Hawaii, 1680 East-West Road, Honolulu, HI 96822, USA. [11]School of Earth, Ocean and Planetary Sciences, Cardiff University, Main Building, Park Place, Cardiff CF10 3YE, UK. [12]P. P. Shirshov Institute of Oceanology of Russian Academy of Sciences, Nakhimovsky prospekt 36, 117997 Moscow, Russia. [13]Department of Petrology, Faculty of Geosciences Utrecht University, Budapestlaan 4, Utrecht, Netherlands. [14]Department of Petrology, Faculty of Earth and Life Sciences, Vrije Universiteit, De Boelelaan 1085, 1081 HV Amsterdam, Netherlands. [15]Department of Earth and Environmental Sciences, University Munich, 80333 Munich, Germany. [16]South Iceland Nature Centre, Strandvegur 50, Vestmannaeyjar, IS 900, Iceland. [17]Department of Earth Science, University of Asmara, Asmara, Eritrea.

*To whom correspondence should be addressed. E-mail: sobolev@geokhi.ru

C), we also plot Mn/Fe and Ni versus Mg/Fe ratios (Fig. 1, B and D). These ratios do not vary significantly with olivine fractionation (see model curves Frac 1 and Frac 2) but nevertheless range considerably (Fig. 1, B and D). Most olivine phenocrysts from MORBs and many from komatiites have Mn and Ni contents similar to those of peridotite-derived melts. In contrast, most olivines from the WPM-THICK group are significantly depleted in Mn and enriched in Ni. Their concentrations are not compatible with the melting products of common peridotites. The olivines from the WPM-THIN group have intermediate Mn and Ni contents.

Concentrations of Ca also provide some discrimination in spite of the greater overlap. Most olivines from the WPM-THICK group are too low in Ca to have precipitated from peridotite-derived melts (shown as experimental-based model compositions and fractionation trajectories, Fig. 1E).

Chromium is strongly controlled by garnet and spinel in peridotites and thus might be useful to decipher products of high-degree melting of peridotite, which leave residuals (restites) free of Cr-rich phases (12). Olivines from Archean komatiites have the highest Cr values and match compositions of olivines from a spinel- and garnet-free refractory restite (Fig. 1F). They could, therefore, be derived directly from high-degree melting of peridotite. In the other groups of olivines, Cr is markedly lower than expected in equilibrium with peridotite at high pressures (see experimental data on lherzolite melting, Fig. 1F). The lowest Cr contents are found in MORB olivines, indicative of residual Cr spinel.

Cobalt (Fig. 2A) shows nearly uniform correlation with Fo for all rock groups, with possibly only minor (around 5%) relative enrichment in WPM-THICK and WPM-THIN over MORB (estimated from group average Co/Fe of table S2a). Decoupling of Co and Ni yields Ni/Co ratios of many WPM-THICK olivines that are unusually high for the Earth mantle (Fig. 2B).

Mn/Fe is the parameter least dependent on olivine fractionation (as shown by the model fractionation curves in Fig. 3). Thus, it is diagnostic of parental magma compositional differences. There is a significant negative correlation of Ni/Mg versus Mn/Fe (linear correlation coefficient r is 0.66 for 238 samples) in spite of strong dependence of Ni/Mg on the degree of olivine fractionation (see fractionation trajectories in Fig. 3A). This correlation improves ($r = 0.88$ for 103 samples) for the subset of olivines with a narrower range of Fo contents (Fo89 to Fo91). MORB olivines are the lowest in Ni and highest in Mn, whereas olivines from the WPM-THICK group are the highest in Ni and lowest in Mn, with olivines from the WPM-THIN group being intermediate.

To minimize the effects of olivine fractionation, we show parameters Ni/(Fe/Mg) and Ca/Fe in Fig. 3, B and C. This procedure also reduces the scatter in the ordinate significantly, thus highlighting the differences between geodynamic settings.

Fate of recycled oceanic crust. In subduction at $P > 2.5$ GPa, the basaltic and gabbroic portions of the oceanic crust are transformed completely to eclogite (clinopyroxene and garnet) with a free SiO_2 phase (13–15). Unless silica has been

Fig. 1. (**A** to **F**) Average compositions of the most highly magnesian olivine phenocrysts in each sample. Concentrations and their ratios are given in ppm versus forsterite content of olivine in mol %. Olivine group names are as defined in text. PM, Herzberg indicates compositions of olivine in equilibrium at 0.1 MPa with melt originally generated at 3.0 to 5.0 GPa from fertile peridotite (12), calculated by Petrolog software (41) for oxygen fugacity corresponding to quartz-fayalite-magnetite (QFM) buffer using the Herzberg model (4), PM, Kinzler, olivine compositions similar to PM, Herzberg but with Ni calculated by using Ni partitioning between olivine and melt from Kinzler et al. (28). Frac 1 is the trend of olivine composition during fractional crystallization from a melt derived from fertile peridotite at 3 GPa and 1515°C (12). Fractionation of olivine modeled up to 20% for oxygen fugacity corresponding to QFM buffer using the Herzberg model (4). Frac 2 is similar to Frac 1 but calculated for 35% crystallization of melt derived at 4.0 GPa and 1630°C (12). Green ellipse indicates field of olivine compositions compatible with peridotitic source. In (F), HRZ, Herzberg stands for calculated compositions of olivine from spinel- and garnet-free harzburgite restite using (4); LHRZ, Walter and HRZ, Walter indicate experimental olivines from lherzolite- and garnet-free harzburgite residual assemblages, respectively, produced by high-pressure melting of fertile peridotite (12). Black ellipse marked "ol + low Ca-Px" indicates field of olivine compositions from refractory garnet- and spinel-free assemblage of olivine and low-Ca pyroxene.
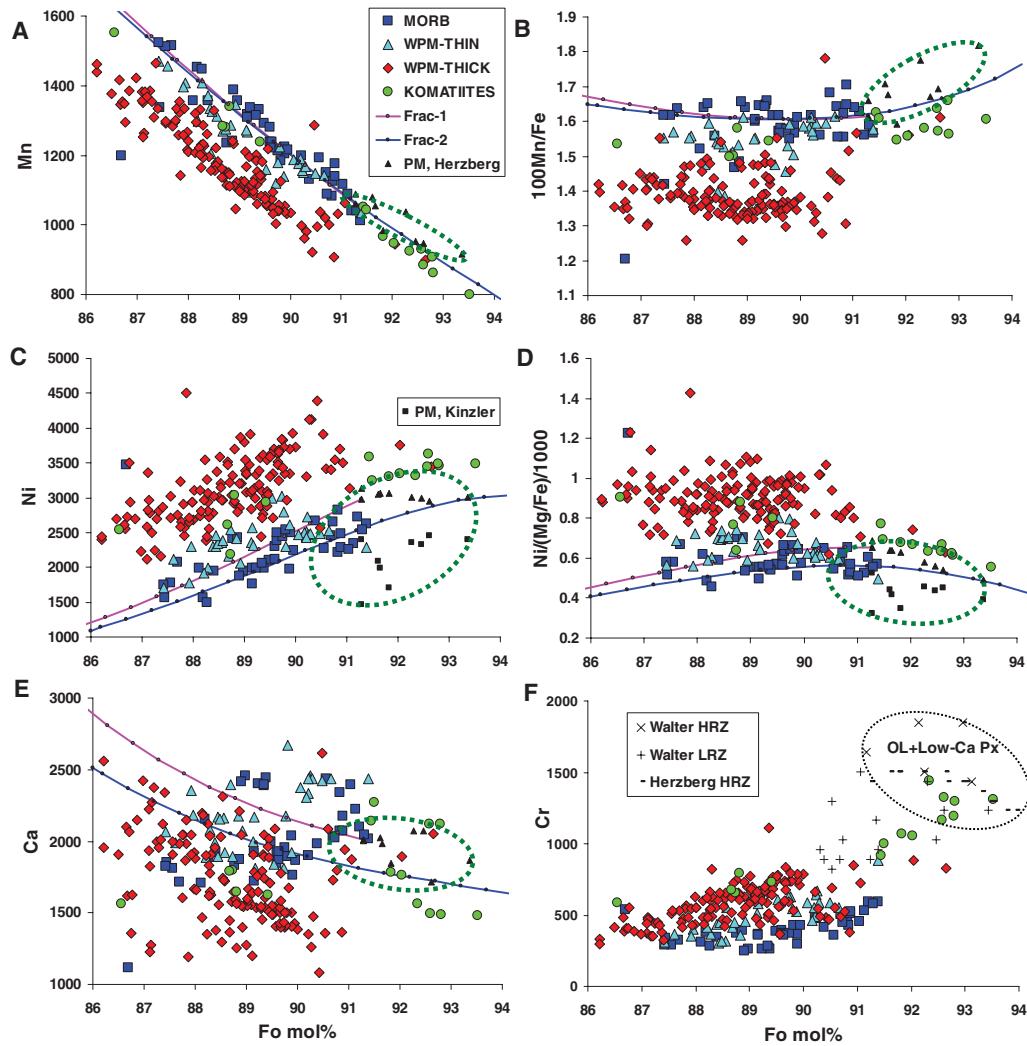
removed during subduction (16), this combination will also be the relevant assemblage during recycling to the upper mantle (17).

In the ascending mantle (e.g., a mantle plume or upstream flow of convecting mantle), the silica-oversaturated eclogite starts melting at higher pressures than the peridotite and produces high silica melt (18, 19). This melt reacts with olivine from peridotite, producing pyroxenes and garnet (5, 8, 19). Previous studies have envisioned that this reaction creates a refertilized peridotite enriched in pyroxene (19, 20). This conclusion would predict variable mixing proportions of individual ingredients (eclogite-derived high-Si melt and peridotite) that are

drastically different in composition. Melting such variable source compositions would create highly nonlinear correlations of $^{187}Os/^{188}Os$ and $^{87}Sr/^{86}Sr$ isotope ratios in the melts, and this is contradicted by the strongly linear correlations observed in Hawaiian basalts (21, 22), which are thought to have a significant eclogite component (3, 5).

However, it has been shown experimentally (23) and proposed on the basis of Korzinskii's theory (24) that, under conditions of local equilibrium, the reaction between high-Si eclogite-derived melt and peridotite produces an olivine-free lithology enriched in pyroxene (5). This fundamentally differs from a partial reaction (19, 20) because it leads to a stable pyroxenite lithology (hybrid py-

roxenite) generated by roughly fixed proportions of high-Si melt and peridotite [constrained by reaction stoichiometry between 40 and 60 weight % (wt %) of melt (5)] irrespective of the initial proportions of the reaction ingredients. Consequently, the hybrid pyroxenite has nearly uniform chemical and isotopic composition, thus constituting a single mixing endmember. Binary mixing of melts derived from peridotite and this pyroxenite leads to near-linear $^{87}Sr/^{86}Sr$ versus $^{87}Os/^{188}Os$ trends (5).

Other predicted geochemical consequences of replacement of olivine by pyroxene are a significant decrease of the bulk distribution coefficient between crystals and melt (K_d) for Ni

Fig. 2. (**A** and **B**) Cobalt and nickel to cobalt ratio versus Fo of average Mg-rich olivine phenocrysts. Pink band at Ni/Co 20 ± 1 represents estimated values for bulk silicate Earth (BSE), core, and chondrites (39). Arrows indicate trend of olivine compositions due to the mantle melting (melting) and magma crystallization (cryst). All other symbols are as on Fig. 1.
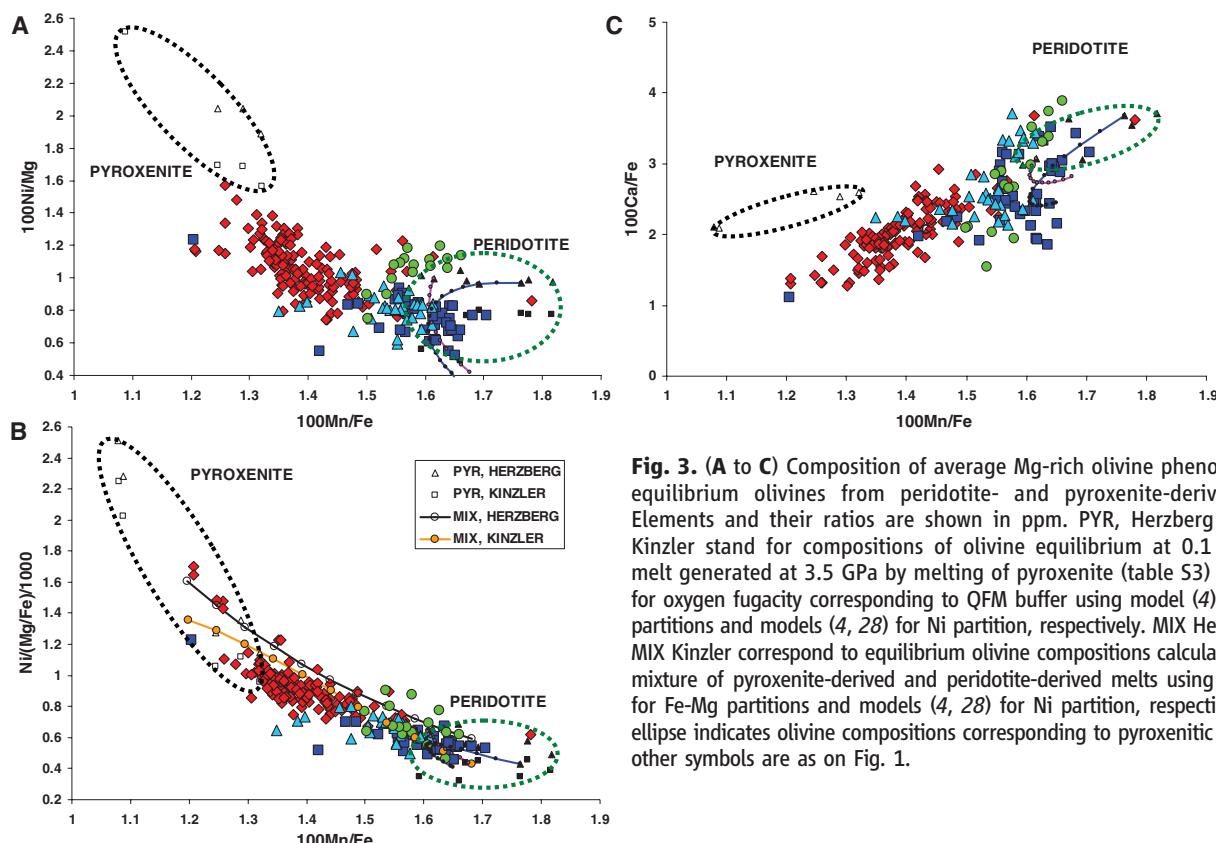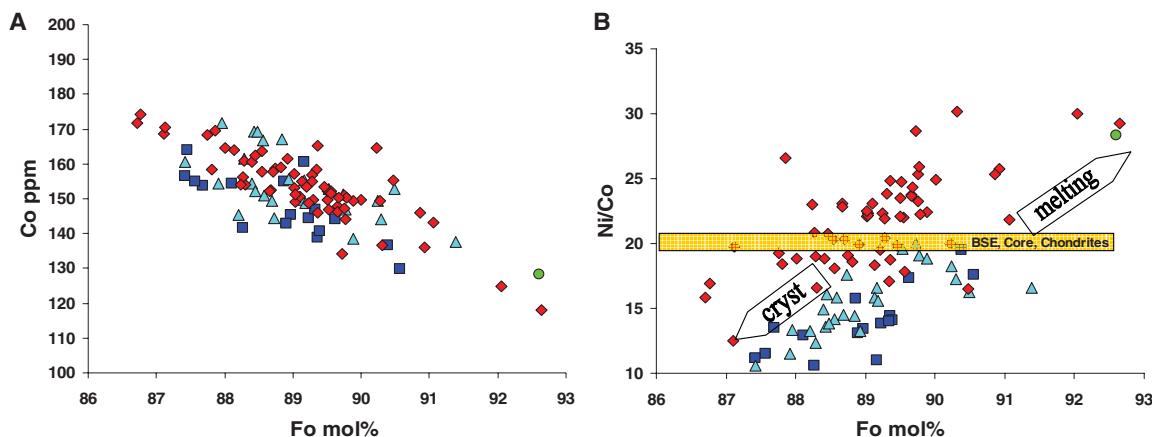
Fig. 3. (**A** to **C**) Composition of average Mg-rich olivine phenocrysts and equilibrium olivines from peridotite- and pyroxenite-derived melts. Elements and their ratios are shown in ppm. PYR, Herzberg and PYR, Kinzler stand for compositions of olivine equilibrium at 0.1 MPa with melt generated at 3.5 GPa by melting of pyroxenite (table S3) calculated for oxygen fugacity corresponding to QFM buffer using model (4) for Fe-Mg partitions and models (4, 28) for Ni partition, respectively. MIX Herzberg and MIX Kinzler correspond to equilibrium olivine compositions calculated for the mixture of pyroxenite-derived and peridotite-derived melts using model (4) for Fe-Mg partitions and models (4, 28) for Ni partition, respectively. Black ellipse indicates olivine compositions corresponding to pyroxenitic source. All other symbols are as on Fig. 1.

(5, 6) and a decrease in the ratio of the bulk coefficients of Mn and Fe (7). These features occur because olivine is the major silicate phase in peridotite concentrating Ni and the only silicate phase in peridotite having K_d for Fe greater than K_d for Mn (7). The bulk K_d changes will increase Ni and lower the Mn/Fe ratio of pyroxenite-derived melt compared with peridotite-derived melts. In addition, melting of pyroxenite yields lower Ca compared with peridotite (8). Additional predicted differences are higher melt fractions for hybrid pyroxenite than peridotite and higher Si and lower Mg in pyroxenite-derived melt (5, 25, 26).

These predictions were tested by experimental melting of a model hybrid pyroxenite (5). Experiments were run at P = 3.5 GPa and temperatures between 1400° and 1570°C in a conventional 1.27-cm piston-cylinder apparatus at the Australian National University (10, 19). These results, together with published experimental data for melting of peridotite (12), confirm the Ni and Mn relationships as well as melting rates predicted above (table S3 and fig. S5). From these data, we calculate equilibrium olivine compositions at low pressure (4, 27, 28) in order to compare them with the natural phenocryst data (Fig. 3). We used these results to estimate mixing proportions of melts derived from the two end-member sources for the olivine data sets representing different geodynamic settings. The end-member melt compositions were calculated from averaging experimental data on melting of pyroxenite and peridotite (10).

Quantitative estimates. We assumed mixtures (in 10% intervals) of the end-member melts (10) and calculated the composition of equilibrium olivines. The calculated mixing trajectories for the two different models for Ni partitioning

are consistent with natural olivine data (Fig. 3B). The relation between Mn/Fe of modeled olivines and mixing proportions (10) was used to compute the amount of pyroxenite-derived component for individual samples (Fig. 4). Olivines from the WPM-THICK group of basalts yield an average of 61 ± 16% (standard deviation) pyroxenite-derived component, similar to results derived from Ni contents in Hawaiian melt inclusions and olivines only (5). The olivines from some continental LIPs (specific suits from Siberia and Karoo) indicate almost pure pyroxenitic sources. Corresponding results for the other groups are for WPM-THIN, 30 ± 13%; for Archean komatiites, 21 ± 10%; and for MORB, excluding one unusual sample from the Southern Atlantic (see below), 17 ± 12% [similar to predictions of (25)]. Because of the uncertainties involved in estimating the end-member compositions, the differences between groups are better constrained than the absolute numbers. Although MORBs contain the lowest proportion of pyroxenite-derived melt, the spread of MORB data is significant, and many samples do contain substantial amounts of pyroxenite-derived component [the extreme is the enriched in silica MORB sample from the Southern Atlantic (29) with 100% pyroxenite-derived component]. The calculations show that the Archean komatiites contain a significant amount of pyroxenitic component (maximum of 30% for samples from Canada and Belingwe), although the largest amount is in Proterozoic komatiitic basalts from Gilmour Island, Canada (up to almost 40%). From these calculations, an estimate of the amount of recycled oceanic crust (10) yields 4% for MORB, 11% for WPM-THIN group, 16% for WPM-THICK group, and around 13% for Archean komatiites. The highest estimate of

the amount of recycled oceanic crust (10) yield Ontong Java high-Mg lavas: 13% to 28%.

Silica-undersaturated basalts. Most of the magmas analyzed in this study are silica saturated (tholeiites or transitional). Only a few samples are moderately silica-undersaturated alkali magmas (e.g., Azores and Afar). Our database is representative of the normal oceanic crust, several of the world's major suites of flood basalts (LIPs), several of the major modern mantle plumes (30), and some komatiites. The strongly silica-undersaturated associations not covered here include continental rift basalts, many smaller ocean islands consisting mostly of alkali lavas, and also some larger-flux plumes (30) such as Pitcairn, Tahiti, and Cape Verde islands. Why are such basalts that are highly enriched in incompatible elements, and therefore presumably generated by very low degrees of melting, nearly always undersaturated in silica? This observation appears to contradict our model; one would expect that silica-saturated melts generated from hybrid pyroxenites should be prevalent, especially at very low melt fractions. There are several possible explanations. (i) A volatile (mostly CO_2-)triggered melting of peridotite may be the dominant mechanism forming strongly silica-undersaturated alkaline magmas at temperatures lower than hybrid pyroxenite melts (31). (ii) Low-degree melts of silica-saturated eclogite may be retained in the source because of their high viscosity, thus preventing production of the hybrid pyroxenite (5). (iii) Melting of hybrid pyroxenite at the contact with peridotite may produce low-degree, silica-undersaturated melts at lower temperatures than melting of hybrid pyroxenite itself (8). (iv) Melting of bimineralic eclogites (no free silica phase) formed from silica-undersaturated recycled crust produces undersaturated alkaline magmas (16).

What controls the amount of pyroxenite-derived melt? By following the method outlined above, we estimated the proportions of melt derived from pyroxenite and peridotite for each parental magma. These proportions depend on several interrelated parameters, namely the thickness of lithosphere, the potential mantle temperature (T_p) (32), and the amount of recycled crust in the upwelling mantle (Fig. 5). Because at the same T_p pyroxenite melts at higher pressure than peridotite (26), a thick lithosphere (which imposes a high lower limit on the depth of melting) will suppress low-depth peridotite melting and therefore favor a high proportion of pyroxenite-derived melts (33, 34). The extreme case is found in some continental flood basalts (specific suites of Siberia and Karoo at table S2a) where the amount of pyroxenite-derived melt is nearly 100%. In such a case, the amount of recycled material cannot be estimated because the peridotitic component contributes no melt. In contrast, a thin lithosphere (MORB, Iceland, Azores, and Detroit seamount) favors a higher proportion of peridotite-derived melt because of the increasing degree of melting of peridotite at shallower depths.
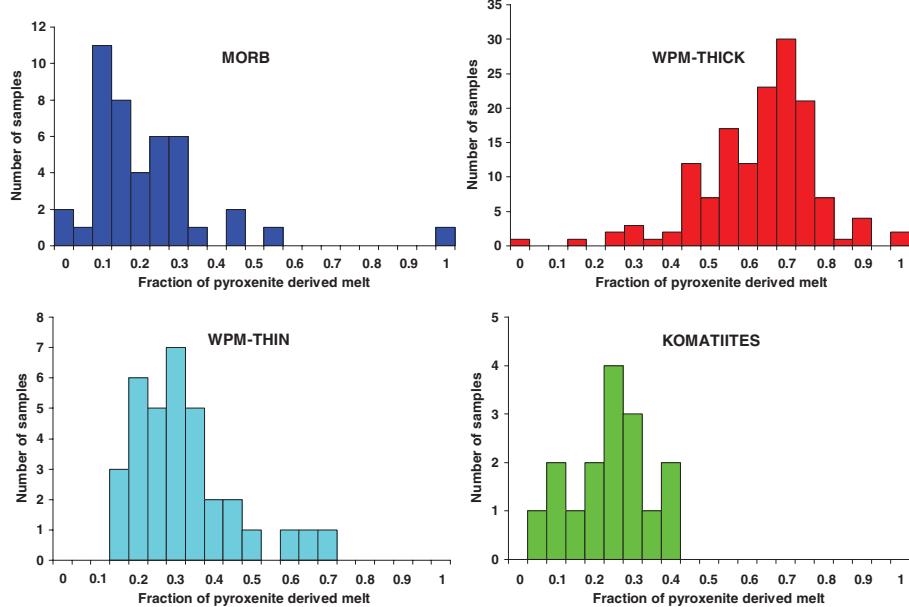

Fig. 4. Estimated amounts of pyroxenite-derived component in the parental melt for 229 samples of four different groups.

A high T_p is an important condition to maintain sufficient buoyancy of mantle plumes or any other upstream mantle flow, and this buoyancy limits the amount of dense eclogite that they can carry (35). Also, a high T_p affects mostly the proportion of peridotite-derived melt because fractional melting imposes a rather stringent upper limit to further melting at high melt fractions (36). High melt fractions are restricted to the eclogite and hybrid pyroxenite assemblages (26) (fig. S5). The peridotite assemblage produces lower melt fractions than pyroxenite (fig. S5) or eclogite (19, 25) at any given temperature and pressure, and its actual extent of melting therefore depends strongly on the specific T_p.

Lastly, why are the proportions of recycled component lower beneath mid-ocean ridges than in thick-lithosphere settings? We suggest several explanations: (i) Relatively low amount of dense recycled component in MORBs is limited by their T_p, which is too low to carry more. (ii) For statistical reasons, plumes are more likely to encounter more-common thick lithosphere than less-common thin lithosphere and few plumes impinge directly on ridges, so we are forced to deal with very-small-number statistics. (iii) Detroit seamount represents one case where a (Hawaiian) plume has encountered thin lithosphere and where our results do indicate a high fraction of recycled crust, similar to those found on the island of Hawaii on the thick lithosphere.

This amount is significantly higher than for Iceland, probably reflecting the effect of a higher T_p of the Hawaiian plume (4). (iv) The surface expression of a plume emplaced under thick lithosphere requires high T_p, which is necessary for carrying a significant amount of recycled crust (35), allowing melts to form at higher pressures than for ordinary peridotite (5, 25, 26), and melting a peridotite at higher pressures [e.g., komatiites (37)].

Heterogeneous versus homogeneous mantle. The model presented here assumes that the recycled crustal component was not fully mixed with peridotite during subduction and mantle convection and thus that the formation of the olivine-free hybrid lithology may take place. On the other hand, homogenization of crustal material within the peridotite mantle should create a range of ultramafic lithologies with variable amounts of olivine, similar to a model by Kelemen et al. (20). Under these circumstances, the major-element contents of partial melts will correspond to the eutectic-like composition, buffered by the peridotite assemblage, whereas the compatible trace elements (Ni and Mn) will be controlled by the bulk partition coefficients of this assemblage and thus by the amount of olivine and pyroxene present in the system. Therefore, the amount of recycled crust can still be estimated on the basis of these trace elements, but their abundances will no longer correlate with the

buffered major elements (Si, Ca, and Al). For Hawaiian basalts, such correlations with Ni are present (5), which requires a strongly heterogeneous source.

Input from Earth's core? The Ni excess in mantle olivines from Siberian LIP (38) and the elevated Fe/Mn ratios in Hawaiian lavas (7) have been explained by input from Earth's core to the sources of mantle plumes. This suggestion is consistent with $^{186}Os/^{188}Os$ ratios for some Hawaiian and Gorgona lavas (39) but is contradicted by the fact that concentrations of highly siderofile (Pt) and chalcophile (Cu) elements reported for Hawaiian basalts are not affected by this process (5). Our olivine data provide strong arguments against any notable core contribution to Ni or Fe excess in the sources of mantle-derived magmas. Cobalt does not show significant excess in olivines (Fig. 2 and fig. S3) and is effectively decoupled from Ni. As a result, the Ni/Co ratio in most Ni-rich mantle plume olivines exceeds 30 at the typical mantle Fo range of 89 to 91 (Fig. 2). This is not expected from a core contribution, because Ni/Co ratios for both mantle and core are almost equal and close to the chondritic value of about 20 (40). In addition, Ca is significantly depleted in many high-Ni and low-Mn olivines from the WPM-THICK group, which cannot be explained by core contribution. Lastly, the olivines from Gorgona komatiites, which do show significant excess in ^{186}Os (39), do not indicate large anomalies in Ni and Mn/Fe, whereas Koolau lavas with the highest Ni excess and lowest Mn/Fe ratio in olivines do not show significant elevations in $^{186}Os/^{188}Os$ ratios (39). This suggests complete decoupling of these potentially strong indicators of core-mantle exchange.

Fig. 5. Schematic model illustrating interplay between amount of recycled crust, thickness of lithosphere, and T_p. Blue, upwelling peridotitic mantle; red, recycled oceanic crust (eclogite with free SiO_2 phase); black dots, melting; yellow, reaction zones forming hybrid pyroxenite; pink, refractory restite after eclogite melting; and green, lithosphere. X_{px}, amount of pyroxenite derived melt in the mixture with peridotite-derived melt, and X_{rc}, amount of recycled oceanic crust in the peridotitic mantle (42).

References and Notes
1. A. W. Hofmann, W. M. White, Earth Planet. Sci. Lett. **57**, 421 (1982).
2. A. W. Hofmann, in The Mantle and Core, vol. 2 of Treatise on Geochemistry, H. D. Holland, K. K. Turekian, Eds. (Elsevier, Amsterdam, 2003), p. 61.
3. E. H. Hauri, Nature **382**, 415 (1996).
4. C. Herzberg, M. J. O'Hara, J. Petrol. **43**, 1857 (2002).
5. A. V. Sobolev, A. W. Hofmann, S. V. Sobolev, I. K. Nikogosian, Nature **434**, 590 (2005).
6. Ni was first proposed as a monitor for replacement of olivine by pyroxene in (20).
7. M. Humayun, L. P. Qin, M. D. Norman, Science **306**, 91 (2004).
8. C. Herzberg, Nature **444**, 605 (2006).
9. S. M. Eggins, Contrib. Mineral. Petrol. **110**, 387 (1992).
10. Materials and methods are available on Science Online.
11. E. J. Jarosevich, J. A. Nelen, J. A. Norberg, Geostand Newsl. **4**, 43 (1980).
12. M. J. Walter, J. Petrol. **39**, 29 (1998).
13. V. S. Sobolev, A. V. Sobolev, Dokl. Akad. Nauk SSSR **237**, 437 (1977).
14. T. Kogiso, M. M. Hirschmann, D. J. Frost, Earth Planet. Sci. Lett. **216**, 603 (2003).
15. T. Kogiso, M. M. Hirschmann, M. Pertermann, J. Petrol. **45**, 2407 (2004).
16. T. Kogiso, M. Hirschmann, Earth Planet. Sci. Lett. **249**, 188 (2006).
17. A. Yasuda, T. Fujii, K. Kurita, J. Geophys. Res. **99**, 9401 (1994).
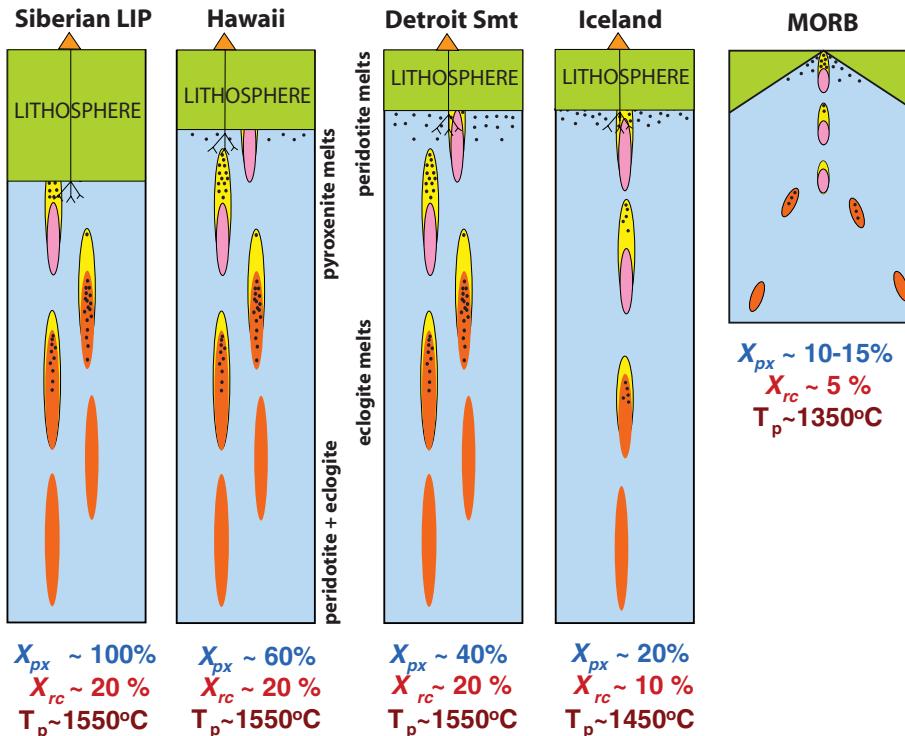18. A. E. Ringwood, D. H. Green, Tectonophysics **3**, 383 (1966).

19. G. M. Yaxley, D. H. Green, *Schweiz. Mineral. Petrogr. Mitt.* **78**, 243 (1998).
20. P. B. Kelemen, S. R. Hart, S. Bernstein, *Earth Planet. Sci. Lett.* **164**, 387 (1998).
21. E. H. Hauri, M. D. Kurz, *Earth Planet. Sci. Lett.* **153**, 21 (1997).
22. J. C. Lassiter, E. H. Hauri, *Earth Planet. Sci. Lett.* **164**, 483 (1998).
23. R. P. Rapp, N. Shimizu, M. D. Norman, G. S. Applegate, *Chem. Geol.* **160**, 335 (1999).
24. D. S. Korzhinskii, *Theory of Metasomatic Zoning* (Clarendon, Oxford, 1970).
25. M. M. Hirschmann, E. M. Stolper, *Contrib. Mineral. Petrol.* **124**, 185 (1996).
26. G. M. Yaxley, *Contrib. Mineral. Petrol.* **139**, 326 (2000).
27. P. Beattie, *Contrib. Mineral. Petrol.* **115**, 103 (1993).
28. R. J. Kinzler, T. L. Grove, S. I. Recca, *Geochim. Cosmochim. Acta* **54**, 1255 (1990).
29. V. S. Kamenetsky *et al.*, *Geology* **29**, 243 (2001).
30. N. H. Sleep, *Annu. Rev. Earth Planet. Sci.* **20**, 19 (1992).
31. G. H. Gudfinnsson, D. C. Presnall, *J. Petrol.* **46**, 1645 (2005).
32. D. McKenzie, M. J. Bickle, *J. Phys. Earth* **38**, 511 (1990).
33. J. P. Morgan, *Geochem. Geophys. Geosystems* **2**, 2000GC000049 (2001).
34. G. Ito, J. J. Mahoney, *Earth Planet. Sci. Lett.* **230**, 29 (2005).
35. M. Pertermann, M. M. Hirschmann, *J. Petrol.* **44**, 2173 (2003).
36. I. Kushiro, *Annu. Rev. Earth Planet. Sci.* **29**, 71 (2001).
37. N. Arndt, *J. Geophys. Res.* **108**, XX (2003).
38. I. D. Ryabchikov, *Dokl. Earth Sci.* **389**, 437 (2003).
39. A. D. Brandon, R. J. Walker, *Earth Planet. Sci. Lett.* **232**, 211 (2005).
40. W. F. McDonough, S. S. Sun, *Chem. Geol.* **120**, 223 (1995).
41. L. V. Danyushevsky, *J. Volcanol. Geotherm. Res.* **110**, 265 (2001).
42. D. McKenzie, M. J. Bickle, *J. Petrol.* **29**, 625 (1988).
43. We thank B. Schulz-Dobrick for supervising purchase and establishing electron microprobe facility in MPI; Hawaiian Scientific Drilling Project team, Koolau Scientific Drilling Project team, Ocean Drilling Program team, A. T. Anderson, E. A. Mathez, and N. Gitahi for providing samples; E. J. Jarosevich for supplying microprobe standards; A. Yasevich for sample preparations and N. Groschopf for maintaining the electron microprobe. The paper benefited from discussions with M. Hirschmann, P. Kelemen, C. Herzberg, B. McDonough, I. Ryabchikov, L. Kogarko, A. Kadik, E. Galimov, V. Batanova. Constructive reviews of C. Herzberg, and P. Kelemen improved the

Genes Required for Mitotic Spindle Assembly in *Drosophila* S2 Cells

Gohta Goshima,[1,3]* Roy Wollman,[2,3] Sarah S. Goodwin,[1] Nan Zhang,[1] Jonathan M. Scholey,[2] Ronald D. Vale,[1,3]† Nico Stuurman[1,3]

The formation of a metaphase spindle, a bipolar microtubule array with centrally aligned chromosomes, is a prerequisite for the faithful segregation of a cell's genetic material. Using a full-genome RNA interference screen of *Drosophila* S2 cells, we identified about 200 genes that contribute to spindle assembly, more than half of which were unexpected. The screen, in combination with a variety of secondary assays, led to new insights into how spindle microtubules are generated; how centrosomes are positioned; and how centrioles, centrosomes, and kinetochores are assembled.

The diamond-shaped mitotic spindle has become one of the most widely recognized images in biology, emblematic of life's propagation through cell division. In higher eukaryotes, the process of spindle formation begins after nuclear envelope breakdown (NEB) when microtubules (MTs), generated both from centrosomes and from the vicinity of chromatin, are organized into a bipolar array (*1–5*). Sister chromatids bind to MTs emanating from opposite poles, are aligned in the middle of the bipolar MT network, and then ultimately separate and move apart during anaphase. Failures early in mitosis result in the formation of an abnormal metaphase spindle, which can lead to mitotic delay and, potentially, chromosome missegregation during the ensuing anaphase.

To understand the mechanism of metaphase spindle assembly, it is critical to identify the proteins required for this process and then dissect how they function. Many mitotic proteins have been identified through genetic and RNAi screens (*6–10*), but the inventory is likely incomplete. Here, we present a genome-wide screen for mitotic spindle morphology in *Drosophila* S2 cells and the functional analysis of unexpected genes discovered through the screen.

Identification of genes involved in metaphase spindle formation by high-throughput microscopy. Because the percentage of S2 cells in mitosis is low (~1%), we conducted our RNAi screen in the presence of dsRNA (double-stranded RNA) to Cdc27 (a subunit of the anaphase-promoting complex) to delay anaphase and thereby increase the percentage of metaphase cells (~10% of the population). Thus, our screen was designed to investigate the assembly of the metaphase spindle, but not anaphase or cytokinesis. We also rescreened the

final hits without Cdc27 RNAi–induced mitotic arrest. The majority (88%) showed identical phenotypes, although a few genes only manifest clear phenotypes under conditions of mitotic arrest (table S1).

Using our custom, full-genome (14,425 genes) *Drosophila* RNAi library (*11*), we treated S2 cells with dsRNA for 4 days, conditions that generally reduce protein levels by >80% (*12, 13*). After dsRNA treatment, cells were fixed and stained for DNA, γ-tubulin, MT, and phospho-histone H3 (pH3) in 96 well plates, and about 40 sites per well were imaged by automated microscopy with a high numerical aperture air objective to obtain relatively high-resolution images of mitotic spindles (Fig. 1A). To reduce the complexity of this large amount of image data, a custom computer code was used to identify, crop, and arrange mitotic spindles into galleries, which were then blindly scored by an observer (Fig. 1B and fig. S1). In addition, computer algorithms measured eight parameters of spindle shape, as well as the intensity of γ-tubulin, cell number, and mitotic index (Fig. 1C) (*11*). More than 4,000,000 spindles were analyzed in this screen.

Before beginning this screen, we annotated 49 genes that produce mitotic defects in S2 cells (table S2). Of these 49 genes, 45 were identified as hits in the primary screen, indicating a high success rate of identifying mitotic phenotypes. However, our final list of genes should not be considered as a complete or universal inventory, because genes can be missed (particularly those with subtle phenotypes), and some phenotypes (or lack thereof) may be specific to S2 cells. False positives by off-target effects of dsRNA can occur in RNAi screens (*14, 15*), so precautions were taken to minimize gene overlap in the dsRNA design, and all unexpected hits were confirmed with another dsRNA that had no overlap with the first dsRNA (*11*). To learn more about the functions of interesting genes,

[1]Howard Hughes Medical Institute and the Department of Cellular and Molecular Pharmacology, University of California, San Francisco, 600 16th Street, San Francisco, CA 94158, USA. [2]Department of Molecular and Cellular Biology, University of California, Davis, One Shields Avenue, 3203 Life Sciences, Davis, CA 95616, USA. [3]Physiology Course, Marine Biological Laboratory, 7 MBL Street, Woods Hole, MA 02543, USA.

*Present address: Institute for Advanced Research, Nagoya University, Furo-cho, Chikusa-ku, Nagoya, 464-8601, Japan.
†To whom correspondence should be addressed. E-mail: vale@cmp.ucsf.edu
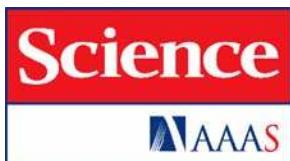
Supporting Online Material for

The Amount of Recycled Crust in Sources of Mantle-Derived Melts

Alexander V. Sobolev, Albrecht W. Hofmann, Dmitry V. Kuzmin, Gregory M. Yaxley, Nicholas T. Arndt, Sun-Lin Chung, Leonid V. Danyushevsky, Tim Elliott, Frederick A. Frey, Michael O. Garcia, Andrey A.Gurenko, Vadim S. Kamenetsky, Andrew C. Kerr, Nadezhda A. Krivolutskaya, Vladimir V. Matvienkov, Igor K. Nikogosian, Alexander Rocholl, Ingvar A. Sigurdsson, Nadezhda M. Sushchevskaya, Mengist Teklay

This PDF file includes:

Materials and Methods
Figs. S1 to S5
Tables S1, S2a, S2b, and S3
References

Other Supporting Online Material for this manuscript includes the following:
available at www.sciencemag.org/cgi/content/full/1138113/DC1

Table S2 (complete) as zipped file

The Amount of Recycled Crust in Sources of Mantle-Derived Melts

A. V. Sobolev, A. W. Hofmann, D. V. Kuzmin, G. M. Yaxley, N. T. Arndt, et al.

Supporting Online Material

Methods and Samples

Electron probe microanalysis. Olivine phenocrysts were analyzed for Si, Fe, Mg, Ca, Ni, Mn, Cr, Al and Co with a Jeol Jxa 8200 electron probe at Max-Planck Institute of Chemistry. Each olivine grain was analyzed in the geometrical center at 20 kV accelerating voltage and probe current of 300 nA. A small olivine subset was analyzed at 30 kV and 200nA. Details of analytical conditions are presented in Table S1. These conditions have been found optimal to obtain best detection limits (see Fig S1). The intensity of the Co Kα line was additionally corrected for overlap with the shoulder of FeK$_\beta$ second order line using the following linear equation established by analyzing Fe bearing standards free of Co:

$$CoO_c = CoO_m - 0.0011 \times FeO_m - 0.013. \qquad [S1]$$

Where CoO_c and CoO_m, FeO_m-are corrected and measured values correspondingly.

The constant in equation [S1] was obtained from analyses of San Carlos olivine standard with known Co content (Table S1). Note that the linear approximation of equation [S1] may not be valid for highly Mg (Fo>93) and low Mg (Fo<70) olivines.

In addition San Carlos olivine standard USNM 111312/444 (S*1*) was run (3 points per each 30-50 measurement points) as an unknown to monitor drifts in calibration and estimate accuracy of analysis. All measurements of Si, Fe, Mn, Ni, Ca and Al were corrected for deviation of this standard from the reference values (Table S1).

For trace elements, the above measurement conditions routinely yield detection limits of around 6-15 ppm based on 3 sigma criteria by Jeol standard software, and errors of 15-30 ppm for trace elements and 0.01 mol% for Fo content (2 standard errors) established by counting statistics and reproducibility of olivine standard (see Fig S1-S2). Precision and

Fig. S2. Reproducibility of San Carlos olivine standard analyzed three times every 30 to 50-th measurement points. Measured- represent uncorrected measurements, corrected – stands for measurements corrected for the calibration drift.

Table S1. Typical analytical conditions of electron probe microanalysis of olivine. Probe current 300 nA, acceleration voltage 20kV.

El	St	Cryst	Line	Peak	BG(+)	BG(-)	S.C.O.
Si	1	TAP	Kα	90	90	-	190740 *
Al	2	TAP	Kα	240	120	120	170 #
Fe	1	LIF	Kα	90	90	-	74230 *
Mn	3	LIFH	Kα	120	60	60	1084 *
Mg	1	TAP	Kα	90	45	45	298040 *
Ca	4	PETJ	Kα	120	60	60	665 #
Ni	5	LIF	Kα	150	70	70	2907 *
Co	6	LIFH	Kα	120	120	-	140 **
Cr	7	PETJ	Kα	120	60	60	95 #

Notes for Table S1: Standards (St) - 1- San-Carlos olivine USNM 111312/444 (S.C.O.); 2-pure Al$_2$O$_3$; 3-Rhodonite; 4-Wollastonite; 5-pure NiO; 6- pure Co-metal; 7-pure Cr$_2$O$_3$. Peak and background (BG) counting time in seconds. *-Accepted values for (S.C.O.) from ref (S*1*) in ppm, **-value measured by LA-ICP MS.

Fig. S1. Detection limit for Mn as function of probe current and peak counting time (in seconds, sec).
Detection limit was determined for San Carlos olivine standard with Jeol software using background statistics and 3 sigma criterion. Typical measurement conditions used in literature are marked as "routine analysis". Analysis at higher beam current and counting times published by (S*3*) is marked as "precision analysis". The analytical conditions used in this study are indicated as "high precision analysis".

Fig. S3. Comparison between Co and Mn concentrations in olivine measured by EPMA and LA-ICPMS. Error bar corresponds to ± 2 standard errors for both EPMA and LA-ICP MS

accuracy of Co and Mn measurements were independently checked by LA-ICP MS analysis using Thermo Finnigan Element 2 mass spectrometer and New Wave Up213 YAG laser (213 nm wavelength) setup. KL2-G (*S4*) and NIST 612 glasses were used as a external standards and Ca in olivine as reference value. Figure S3 shows that both Co

Table S2f. These tables are included as separate spreadsheets together with Table S2a in the Excel file called Table S2. Table S2a is also placed in the end of this file. Tables S2c,d,e,f include concentrations of oxides and their relative standard deviations in % (signal counting statistics) for individual olivine grains. Each analytical point in addition to

Melting of pyroxenites. The model hybrid pyroxenite composition from Sobolev et al. (*S3*) (their Table S2, column 50%) was chosen for the high pressure experimental investigation. A synthetic starting material with this composition (Px-1) was prepared for the experiments by blending high purity oxides and carbonates under analytical grade
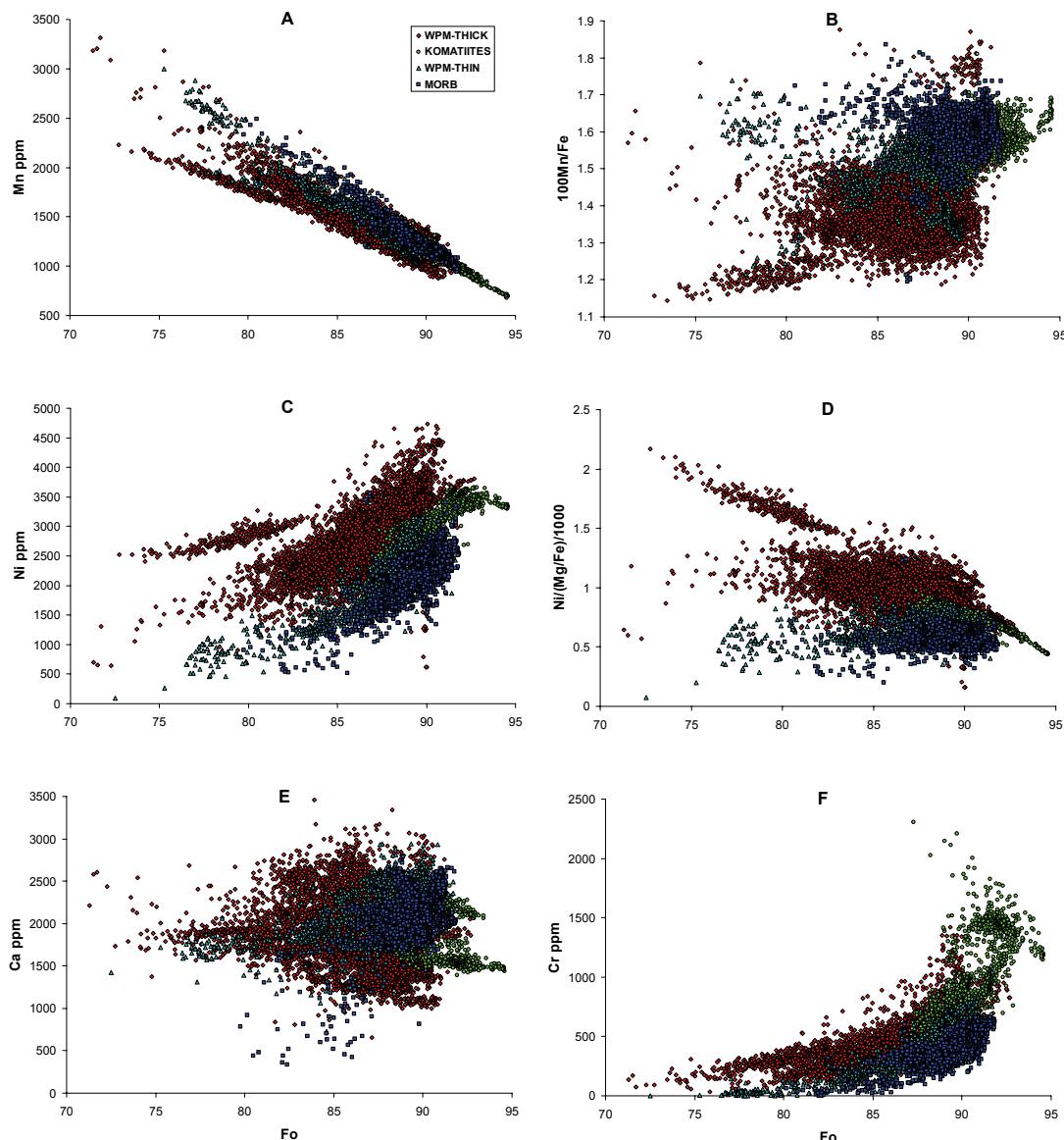
Fig. S4. Composition of olivine phenocrysts: all data from database. Group of MORB olivines shown on top of all groups.

and Mn concentrations measured by EPMA correspond to those analyzed by LA-ICP MS within 20 ppm (2 standard errors).

Olivine database. The averaged most highly magnesian olivines for each sample are presented in Table S2a. Individual olivine analyses are presented on Fig S4 and in Tables S2,c,d,e,f separately for each group: MORB in Table S2c, WPM-THIN in Table S2d, WPM-THICK in Table S2e and KOMATIITES in

sample name has a unique number. Table S2a includes group title, sample name, reference for sample description (if published), information on locality, number of averaged high-Mg grains, forsterite content, element concentrations in ppm, standard errors of the mean in ppm, characteristic ratios of elements and calculated amount of pyroxenitic component (X_{px}, see below for explanation).

acetone for several hours, until the material was homogenous and very fine-grained. The resultant dried powder was then pelletised and fired for 12 hours at 1100°C to decarbonate and partially fuse the components. FeO was added after firing in the form of synthetic fayalite (Fe_2SiO_4), and again blended under acetone. The final mixture was then dried overnight at 200°C and subsequently stored at 110°C. The actual composition of the Px-1

starting material was checked by electron probe microanalysis of quenched glass prepared by fusing the starting mix at 1300°C in an Ar atmosphere in a box furnace and quenching in water (Table S3).

High pressure experiments were run at a pressure of 3.5 GPa and temperatures between 1400-1570°C in a conventional 1.27cm piston-cylinder apparatus at the Australian National University. The Px-1 starting material (≈1 mg) was loaded into graphite capsules, which were sealed by arc-welding in Pt outer capsules. The

capsules were placed centrally into NaCl-pyrex sleeves with MgO inserts, an assembly which requires no friction correction. Type B thermocouples ($Pt_6Rh_{94}/Pt_{30}Rh_{70}$) were employed, with the thermocouple join placed within a fraction of a millimeter of the Pt capsule. Runs were brought to run temperature and pressure simultaneously. Temperature was controlled throughout by Eurotherm controllers attached to the thermocouple and is accurate to ±10°C. Pressure is accurate to ±0.1 GPa. Experiments were maintained at the

desired PT condition long enough to allow a close approach to equilibrium, and then quenched by terminating power to the furnace.

After recovery from the post-run assembly, the Pt capsules were mounted in 1 inch diameter epoxy buttons, sectioned longitudinally and polished, in preparation for analysis by scanning electron microscopy at the Australian National University and electron probe microanalysis at the Max Planck Institute for Chemistry in Mainz.

Table S3. Proportions of phases produced and melt compositions from melting of pyroxenite at 3.5 GPa and 1400-1575°C.

Run	DT	T	Phases proportions, wt%				Melt compositions in oxide wt%, Ni in ppm										
N	h	° C	melt	Opx	Cpx	Ga	SiO_2	TiO_2	Al_2O_3	FeO	MnO	MgO	CaO	Na_2O	K_2O	Cr_2O_3	Ni
C-2298	45	1400	8	0.	79	14	60.70	2.76	14.40	6.80	0.068	4.44	7.71	2.34	0.70	0.07	453
C-2317	48	1450	16	0	71	12	55.76	2.33	14.20	7.63	0.081	7.45	7.95	2.16	0.44	0.06	626
C-2301	5	1500	33	0	60	6	53.30	1.58	14.21	8.25	0.106	10.67	8.61	1.75	0.13	0.09	810
C-2330	5	1520	42	0	55	3	52.54	1.29	14.22	8.65	0.112	11.66	8.65	1.98	0.14	0.11	850
C-2332	5	1540	72	24	4	0	52.00	0.86	13.55	8.19	0.125	14.08	9.00	1.80	0.08	0.20	796
C-2318	6	1550	76	18	7	0	52.38	0.83	13.39	7.95	0.117	14.67	8.77	1.74	0.09	0.20	843
C-2319	5	1575	79	20	0	0	52.20	0.79	13.07	8.11	0.126	15.44	8.52	1.67	0.07	0.22	841
Px-1, Bulk composition							52.67	0.64	11.26	7.55	0.119	18.48	7.05	1.52	0.06	0.25	1000
Peridotite-derived endmember							46.79	0.85	11.50	9.68	0.185	19.07	10.00	0.84	0.47	0.39	642
Pyroxenite -derived endmember							52.56	1.07	13.71	8.24	0.117	13.32	8.72	1.79	0.10	0.16	830

Note for Table S3: Melt, Opx, Cpx, Ga, - proportions of melt, orthopyroxene, clinopyroxene and garnet in experimental runs in mass fractions, calculated using list square method from bulk composition and compositions of phases. DT- run duration in haurs, T- temperature in °C. The amount of Ni has been calculated using the method described in Sobolev et al, 2005 (S3). This method uses known phase proportions and the distribution of Ni between phases, to calculate Ni in the phases on the basis of mass balance and known bulk Ni content. The assumed bulk Ni concentrations are: 1000 ppm for pyroxenite (Px-1) and 1900 ppm for peridotite (S3).
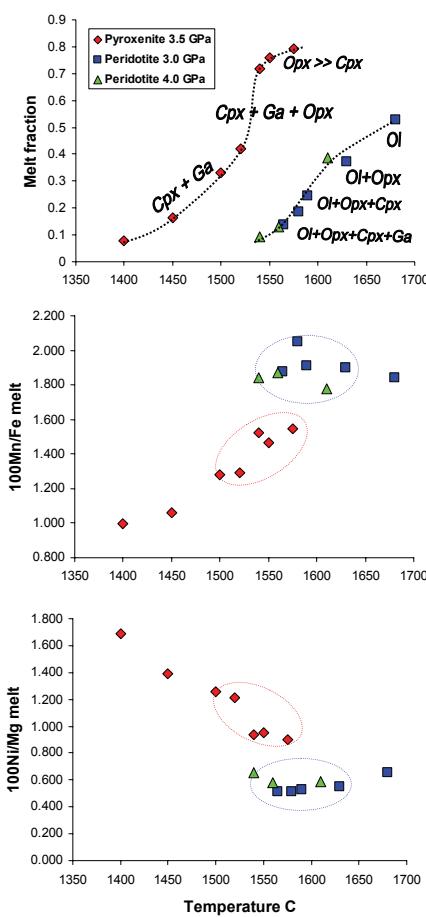
Pyroxenite-derived component in melts. In order to estimate endmember compositions we have averaged compositions of melts of pyroxenite and peridotite (see Fig.S5). For pyroxenite we averaged all melt compositions except numbers C-2298 and C-2327 (Table S3) produced at low temperature and low percentage of melting. For peridotites we averaged 7 compositions of melts from runs 30.12, 30.07, 30.14, 30.1 (3.GPa), 40.06, 40.07, 40.05 (4.GPa) of Walter, 1998 (S2). The endmember compositions are shown in Table S3. We assumed that the mixtures consist of endmembers with similar temperatures, and we therefore excluded (from the averaging procedure) experimental melts with very low or very high temperatures (see Fig.S5).

The calculated endmember melts were then mixed (in 10% intervals) producing mixed melt compositions. For these melts the composition of equilibrium olivines were

Fig. S5. Melt fraction and composition of experimental melts of pyroxenite and fertile peridotite. Temperatures for experimental runs of fertile peridotite (S2) are extrapolated to 3.5 GPa by using slope 100C/GPa. Data for pyroxenite from Table S3. Crystalline phase coexisting with melt are: Ol - olivine; Opx - orthopyroxene; Cpx - clinopyroxene; Ga - garnet. Blue and red ellipses indicate analyses averaged to calculate peridotite-derived and pyroxenite-derived endmembers respectively.

calculated using Herzberg's model (S5). The calculated Mn/Fe ratios of the olivines and the amounts of pyroxenitic endmember (X_{px}) yield a straight line:

$$X_{px} = 3.48 - 2.071 \times (100Mn/Fe) \quad [S2]$$

We used this equation to calculate the amount of pyroxenitic endmember for each average olivine composition in Table S2a.

The calculated endmember compositions are derived from experiments at high pressures and temperatures. Therefore, they are directly relevant primarily to thick-lithosphere settings, but we have applied them for all settings. Equivalent estimates for lower pressures and temperatures (1.0 GPa and 1300-1350°C) have been calculated using pMELTS (S6). This yielded similar degrees of melting and residual assemblages (50 to 60% of melting and low-Ca pyroxene dominated residue) as those derived from high pressure and temperature runs (Table S3). This gives us some confidence that the same Mn/Fe ratios can be applied to lower pressures, but experimental confirmation will be needed. Additional confidence in the results is derived from the observation that the extreme compositions observed in both MORB and WPM-thick settings match the calculated endmember compositions reasonably well.

Oceanic crust in magma sources. A final step is to estimate the actual amount of recycled oceanic crust (X_{crc}) from the determined proportion of pyroxenite-derived melt. This quantity is linked to the proportion of hybrid pyroxenite-derived melt (X_{px}) by the degree of melting of eclogite (F_e), the amount of eclogite-derived melt needed to produce hybrid pyroxenite from peridotite (X_e), and the degrees of melting of peridotite (F_{pe}) and pyroxenite (F_{px}) (S3):

$$X_{crc} = \frac{X_e}{F_e(\frac{1-X_{px}}{X_{px}}\frac{F_{px}}{F_{pe}} + \frac{1-F_e}{F_e}X_e + 1)} \qquad [S3]$$

Following assumption of Sobolev et al, (2005) (S3), we propose that the extent of melting of eclogites reaches a maximum of 50%. This limit is unlikely to be exceeded significantly during fractional melting, because this process removes Na (S7) and thereby renders the residue highly refractory. Therefore it is also not strongly dependent on the potential temperature of the rising mantle material. The amount of pyroxenite produced by reaction of the primary (eclogite-derived) melt with peridotite is prescribed by the stoichiometry of the reaction, which also yields proportions of the reactants of close to 50:50 (S3). For these, proportions, the amount of reaction pyroxenite equals the amount of initial eclogite. The melt fraction produced by the pyroxenite can be estimated at low pressure (1-2 GPa by modeling using pMELTS software (S6)), yielding a maximum of about 60 % for batch melting at 1 GPa and 1320 to 1350°C. At higher pressures (3.5 GPa) we must rely on the experimental data (Table S3, Fig. S5), which also yield a maximum melt fraction of about 50-60% for batch melting for 1540-1550°C.

These values will be significantly lower for fractional melting (S8), for the same reason as discussed for eclogite melting (i.e. early Na removal). Adopting an amount of 50 % pyroxenite melting will therefore result in a minimum estimate in the amount of recycled crust present. Finally, we estimate the melt fraction of peridotite using published models (S5) for MORB (10%), Iceland, as a proxy for the WPM-THIN group (20%), Hawaii, as proxy for the WPM-THICK group (10%) and Archaean komatiites -40% (S9). This yields the following average estimates for the amounts of recycled oceanic crust in the mantle sources: 4% for MORB, 11% for WPM-THIN group, 16% for WPM-THICK group, and around 13% for Archean komatiites. According to (S10) the melt fraction of peridotite for Ontong Java high-Mg magmas corresponds to 30%, which yield the amount of recycled oceanic crust of 13-28% in the mantle source of these magmas.

Supporting Online References

S1. E. J. Jarosevich, J. A. Nelen, J. A. Norberg, *Geostand. Newsl.* **4**, 43 (1980).

S2. M. J. Walter, *Journal of Petrology* **39**, 29 (J1998).

S3. A. V. Sobolev, A. W. Hofmann, S. V. Sobolev, I. K. Nikogosian, *Nature* **434**, 590 (2005).

S4. K. P. Jochum *et al.*, *Geostandards Newsletter-the Journal of Geostandards and Geoanalysis* **24**, 87 (2000).

S5. C. Herzberg, M. J. O'Hara, *Journal of Petrology* **43**, 1857 (2002).

S6. M. S. Ghiorso, M. M. Hirschmann, P. W. Reiners, V. C. Kress, *Geochemistry Geophysics Geosystems* **3** (2002).

S7. T. Kogiso, M. Hirschmann, *Earth and Planetary Science Letters* **249**, 188 (2006).

S8. I. Kushiro, *Annual Review of Earth and Planetary Sciences* **29**, 71 (2001).

S9. N. Arndt, *Journal of Geophysical Research-Solid Earth* **108** (2003).

S10. J. G. Fitton, M. Godard, in *Origin and Evolution of the Ontong Java Plateau*J. G. Fitton, J. J. Mahoney, P. J. Wallace, A. D. Saunders, Eds. (Geological Society, London, Special Publication, 229 London, 2004) pp. 151-178.

S11. B. Sylvander, D. M. Christie, L. V. Danyushevsky, in *Eos.* (1996), vol. 77, pp. F691.

S12. M. R. Perfit *et al.*, *Earth and Planetary Science Letters* **141**, 91 (1996).

S13. A. V. Sobolev, *Petrology* **4**, 209 (1996).

S14. V. S. Kamenetsky *et al.*, *Earth and Planetary Science Letters* **160**, 115 (1998).

S15. V. Kamenetsky, *Earth and Planetary Science Letters* **142**, 479 (1996).

S16. A. P. Leroex, H. J. B. Dick, L. Gulen, A. M. Reid, A. J. Erlank, *Geochimica Et Cosmochimica Acta* **51**, 541 (1987).

S17. V. S. Kamenetsky *et al.*, *Geology* **29**, 243 (2001).

S18. N. M. Sushchevskaya *et al.*, *Geochemistry International* **43**, 222 (2005).

S19. in Table S2b.

S20. T. Elliott, J. Blichert-Toft, A. Heumann, G. Koetsier, V. Forjaz, *Geochimica Et Cosmochimica Acta* **71**, 219 (2007).

S21. S. Huang, M. Regelous, T. Thordarson, F. A. Frey, *Geochemistry Geophysics Geosystems* **6** (2005).

S22. A. C. Kerr, R. W. Kent, B. A. Thomson, J. K. Seedhouse, C. H. Donaldson, *Journal of Petrology* **40**, 873 (1999).

S23. G. M. Yaxley, V. S. Kamenetsky, M. Kamenetsky, M. D. Norman, D. Francis, *Contributions to Mineralogy and Petrology* **148**, 426 (2004).

S24. L. M. Larsen, A. K. Pedersen, *Journal of Petrology* **41**, 1071 (2000).

S25. K. G. Cox, B. G. Jamieson, *Journal of Petrology* **15**, 269 (1974).

S26. Y. G. Xu, S. L. Chung, B. M. Jahn, G. Y. Wu, *Lithos* **58**, 145 (2001).

S27. S. L. Chung, B. M. Jahn, *Geology* **23**, 889 (1995).

S28. M. Teklay, A. W. Hofmann, G. E. Brugmann, J. C. Lassiter, *Geochimica Et Cosmochimica Acta* **66**, A767 (2002).

S29. A. V. Sobolev, I. K. Nikogosian, *Petrology* **2**, 111 (1994).

S30. J. M. Rhodes, M. J. Vollinger, *Geochemistry Geophysics Geosystems* **5**, Q03G13 (2004).

S31. F. A. Frey *et al.*, *Journal of Geophysical Research-Solid Earth and Planets* **96**, 14347 (1991).

S32. F. A. Frey, M. O. Garcia, M. F. Roden, *Geochimica Et Cosmochimica Acta* **58**, 1441 (1994).

S33. E. H. Haskins, M. O. Garcia, *Contributions to Mineralogy and Petrology* **147**, 162 (2004).

S34. M. D. Norman, M. O. Garcia, *Earth and Planetary Science Letters* **168**, 27 (1999).

S35. M. O. Garcia, D. J. P. Foss, H. B. West, J. J. Mahoney, *Journal of Petrology* **36**, 1647 (1995).

S36. V. V. Matvienkov, O. G. Sorokhtin, *Okeanologiya* **38**, 742 (1998).

S37. A. A. Gurenko *et al.*, *Chemical Geology* **233**, 75 (2006).

S38. A. A. Gurenko, T. H. Hansteen, H.-U. Schmincke, in *Proceedings of the Ocean Drilling Program, Scientific Results* P. P. E. Weaver, H.-U. Schmincke, J. V. Firth, W. Duffield, Eds. (1998), vol. 157, pp. 375-401.

S39. N. T. Arndt, A. J. Naldrett, D. R. Pyke, *Journal of Petrology* **18**, 319 (1977).

S40. N. T. Arndt, *Journal of Petrology* **27**, 279 (1986).

S41. M. J. Bickle *et al.*, in *The geology of the Belingwe Greenstone Belt, Zimbabwe* M. J. Bickle, E. G. Nisbet, Eds. (Balkema, Rotterdam, 1993) pp. 175-214.

S42. N. T. Arndt, G. E. Brügmann, K. Lehnert, C. Chauvel, B. W. Chappell, in *Geochemistry and Mineralization of Proterozoic Volcanic Suites* T. C. Pharaoh, R. D. Beckinsale, D. Rickard, Eds. (Geol. Soc. Spec. Publ., 1987) pp. 133-145.

S43. A. C. Kerr, *Lithos* **84**, 77 (2005).

Table S2b. Locations (GPS coordinates) and description for Icelandic samples

Sample	Locality	Description	latitude	longitude
01-7	Reykjanes, Haleyjabunga	Glassy olivine phyric picrite	N63° 48.954'	W22° 38.646'
03-102	Reykjanes, Lagafell	Glassy olivine phyric picrite	N63° 52.906'	W22° 32.611'
03-106	Reykjanes, Haleyjabunga	Glassy olivine phyric picrite	N63° 48.873'	W22° 38.724'
01-15	Reykjanes, Sulur	Glassy olivine –phyric basalt	N63° 54.094'	W22° 32.558'
01-12	Reykjanes, Stapafell	Glassy olivine-plagioclase phyric picrite	N63° 54.601'	W22° 31.370'
01-8	Hengill, Midfell	Glassy olivine phyric picrite with rare plagioclase and clinopyroxene xenocrysts	N64° 10.140'	W21° 04.257'
01-10	Hengill, Midfell	Glassy olivine phyric picrite with rare plagioclase and clinopyroxene xenocrysts	N64° 10.103'	W21° 04.118'
01-19	Hengill, Maelifell	Glassy olivine phyric basalt with rare plagioclase and clinopyroxene xenocrysts	N64° 06.252'	W21° 10.744'
03-131	Kistufell	Glassy olivine phyric basalt	N64° 47.806'	W17° 13.745'
03-164	Kistufell	Glassy olivine phyric basalt	N64° 46.918'	W17° 12.713'
03-140	Kistufell	Glassy olivine phyric basalt	N64° 47.861'	W17° 12.202'
03-161	Kistufell	Glassy olivine phyric basalt	N64° 47.808'	W17° 13.957'
01-55	Theistareykir, Laufrandarhraun	Glassy olivine phyric picrite	N65° 56.285'	W17° 05.047'
01-57-4	Theistareykir, Laufrandarhraun	Glassy olivine phyric picrite	N65° 55.791'	W17° 04.463'
01-56-1	Theistareykir, Laufrandarhraun	Glassy olivine phyric picrite	N65° 56.277'	W17° 05.374'
01-41	Theistareykir, Theistareykjahraun	Glassy olivine phyric basalt	N65° 57.547'	W17° 04.120'
01-44	Theistareykir, Laufrandarhraun	Glassy olivine phyric picrite	N65° 56.068'	W17° 05.246'
01-56-2	Theistareykir, Laufrandarhraun	Glassy olivine phyric picrite	N65° 56.277'	W17° 05.374'
01-54	Theistareykir, Laufrandarhraun	Glassy olivine phyric picrite	N65° 56.281'	W17° 04.624'
01-51	Theistareykir, Langavitishraun	Glassy olivine phyric basalt with rare clinopyroxene phenocrysts	N65° 56.058'	W16° 52.282'
03-224	Snaefellsness, Enni	Glassy olivine phyric basalt	N64° 54.146'	W23° 45.776'
03-226	Snaefellsness, Sydri-Raudamelur	Olivine phyric basalt	N64° 52.296'	W22° 17.368'
03-220	Snaefellsness, Ytri-Raudamelur	Olivine phyric basalt	N64° 52.717'	W22° 20.860'

Table S2a. Average compositions of most Mg-rich olivine phenocrysts (see text of paper for definition).

GROUP	Geodynamic setting	References	Sample	Geographic	Locality	N	Fo	Al ppm	Fe ppm	Mn ppm	Mg ppm	Ca ppm	Ni ppm	Co ppm	Cr ppm	100*Mn/Fe	100*Ni/Mg	Ni/(Mg.Fe)/1000	100Ca/Fe	X px Mn/Fe	STE Fo wt%	Al ppm	Fe ppm	Mn ppm	Mg ppm	Ca ppm	Ni ppm	Co ppm	Cr ppm
MORB	MORB	(S11)	I13-16	Indian Ocean	105.22 oE SEIR	24	89.49	270	79979	1293	296327	1995	2109		389	1.617	0.712	0.569	2.494	0.135	0.07	7	502	10	268	13	38		5
MORB	MORB	(S11)	I45-3	Indian Ocean	116.72 oE SEIR	9	89.90	298	77032	1224	298238	1761	2500		369	1.590	0.838	0.646	2.285	0.191	0.05	4	422	8	234	9	27		9
MORB	MORB	unpb	30-29	Indian Ocean	124.28 oE SEIR	10	89.60	236	79185	1280	296874	1843	2115		390	1.617	0.712	0.564	2.328	0.135	0.10	10	724	14	499	20	71		8
MORB	MORB	(S11)	144-13	Indian Ocean	115.21 oE SEIR	29	89.16	269	82315	1316	294471	1921	1993		363	1.599	0.677	0.557	2.334	0.171	0.05	6	377	8	265	20	39		5
MORB	MORB	unpb	18-10	Indian Ocean	126.74 oE SEIR	24	89.60	272	78878	1239	295854	1921	2303		372	1.571	0.778	0.614	2.435	0.229	0.06	4	438	8	280	12	38		7
MORB	MORB	(S11)	69-1	Indian Ocean	88.92 oE SEIR	11	89.89	319	76966	1205	297733	2036	1972		299	1.566	0.662	0.510	2.646	0.239	0.05	10	417	8	287	10	29		4
MORB	MORB	(S11)	88-22	Indian Ocean	96.83 oE SEIR	10	88.18	213	88627	1453	287837	2153	1572		380	1.639	0.546	0.484	2.429	0.088	0.11	8	755	14	526	10	18		7
MORB	MORB	unpb	5-2	Indian Ocean	127.58 oE SEIR	33	89.63	257	78288	1238	294600	1875	2383		364	1.582	0.809	0.633	2.395	0.207	0.04	3	307	6	235	3	17		2
MORB	MORB	unpb	16-19	Indian Ocean	127.58 oE SEIR	18	88.40	235	87179	1357	289113	1920	1953		348	1.557	0.676	0.589	2.202	0.258	0.15	3	1112	18	675	21	48		6
MORB	MORB	unpb	J-PE-1	Pacific Ocean	Garrett F.Z.	32	90.82	395	69627	1084	299751	2071	2817		480	1.557	0.940	0.654	2.975	0.259	0.02	10	171	3	169	3	38		11
MORB	MORB	(S12)	SG-1	Pacific Ocean	Siqueiros F.Z.	89	90.38	377	72454	1131	296261	1985	2661	137	413	1.561	0.898	0.651	2.739	0.250	0.03	4	191	4	201	2	15	1	5
MORB	MORB	(S13)	FZ 649-5(i)	Atlantic Ocean	9 N MAR	36	89.75	301	76919	1213	293090	1953	2444		374	1.577	0.834	0.642	2.539	0.216	0.04	5	309	4	200	5	15		4
MORB	MORB	(S13)	FZ 649-5(ii)	Atlantic Ocean	9 N MAR	28	88.76	302	84161	1235	289205	1832	2410		371	1.467	0.833	0.701	2.177	0.444	0.04	7	276	6	173	14	30		6
MORB	MORB	(S13)	649(i)	Atlantic Ocean	9N MAR	12	89.63	314	78044	1222	293379	1929	2501	144	360	1.566	0.853	0.665	2.472	0.239	0.05	7	410	6	334	18	20	2	5
MORB	MORB	(S13)	649(ii)	Atlantic Ocean	9N MAR	30	88.87	310	83452	1240	288834	1875	2434	155	390	1.486	0.840	0.701	2.247	0.406	0.08	9	639	10	585	20	55	5	3
MORB	MORB	(S13)	All-60, Stn9, D9, 9-20	N. Atlantic	43N MAR	88	89.81	332	76416	1184	293134	1896	2543		430	1.549	0.868	0.663	2.481	0.274	0.02	2	152	2	103	2	11		3
MORB	MORB	unpb	All-32 11-92	N. Atlantic	43N MAR	92	90.70	242	70116	1151	297618	2032	2461		502	1.642	0.827	0.580	2.898	0.082	0.01	5	109	2	97	9	7		5
MORB	MORB	unpb	All-32 12-6(i)	N. Atlantic	43N MAR	74	90.83	240	69316	1124	298835	2340	2221		428	1.622	0.743	0.515	3.376	0.124	0.03	3	200	3	134	14	19		10
MORB	MORB	unpb	All-32 12-6(ii)	N. Atlantic	43N MAR	13	90.88	252	68934	1175	298950	2174	2291		510	1.705	0.766	0.528	3.153	-0.048	0.01	3	57	2	166	33	10		3
MORB	MORB	unpb	All-32 12-2	N. Atlantic	43N MAR	85	91.13	254	66863	1089	298972	2221	2339		531	1.629	0.782	0.523	3.321	0.110	0.03	4	201	4	132	27	18		10
MORB	MORB	(S14)	All-32 12-7	N. Atlantic	43N MAR	55	91.03	213	67956	1115	300251	2393	2252		453	1.641	0.750	0.510	3.522	0.084	0.03	4	211	4	152	22	11		10
MORB	MORB	(S15)	All-32 11-178	N. Atlantic	43N MAR	68	90.88	260	69155	1140	299897	2072	2479		521	1.648	0.827	0.572	2.996	0.070	0.03	5	202	3	126	12	15		6
MORB	MORB	(S15)	CH-31 Dr08 695	N. Atlantic	Famous	17	91.21	306	66586	1039	300597	2100	2721		592	1.561	0.905	0.603	3.154	0.251	0.09	9	670	12	371	8	81		8
MORB	MORB	(S15)	CH-31 Dr08 136-02	N. Atlantic	Famous	19	91.38	298	64581	1012	297930	2019	2620		595	1.567	0.879	0.568	3.127	0.237	0.07	10	523	9	265	7	89		8
MORB	MORB	(S15)	ARP-73 10.03	N. Atlantic	Famous	52	91.30	295	65425	1039	298895	2046	2535		582	1.589	0.848	0.555	3.126	0.193	0.05	7	345	5	180	5	31		3
MORB	MORB	(S16)	AG32 4-68	S. Atlantic	Bouvet	44	90.72	319	69996	1088	297891	2024	2653		450	1.554	0.891	0.623	2.891	0.264	0.04	7	270	5	185	4	41		10
MORB	MORB	unpb	AG-32 3-36	S. Atlantic	Bouvet	98	89.95	282	75474	1217	294027	1869	2239		427	1.612	0.761	0.575	2.476	0.144	0.04	4	264	4	156	4	40		6
MORB	MORB	(S17)	AG-32 3-41	S. Atlantic	Bouvet	73	90.22	301	74107	1199	297481	1902	2432		474	1.618	0.818	0.606	2.566	0.132	0.02	5	149	3	122	10	35		7
MORB	MORB	unpb	518-60/1	S. Atlantic	Bouvet	5	86.70	225	99549	1199	282320	1115	3478		536	1.204	1.232	1.226	1.120	0.99	0.05	6	308	6	345	11	24		22
MORB	MORB	unpb	13-12/49a	Atlantic Ocean	Romanche F.Z.	60	89.35	198	80862	1332	295314	2392	1999	139	270	1.648	0.677	0.547	2.958	0.070	0.03	3	230	4	206	4	13	1	6
MORB	MORB	unpb	13-12/49c	Atlantic Ocean	Romanche F.Z.	58	88.99	198	82768	1357	290684	2455	1953	145	264	1.640	0.672	0.556	2.966	0.087	0.04	5	268	5	170	13	13	1	16
MORB	MORB	unpb	13-12/49d	Atlantic Ocean	Romanche F.Z.	19	88.90	185	83795	1388	291945	2415	1872	143	250	1.656	0.641	0.537	2.881	0.053	0.06	7	415	7	229	31	18	2	10
MORB	MORB	unpb	13-12/49e	Atlantic Ocean	Romanche F.Z.	36	87.69	185	92539	1514	286753	1715	2076	154	322	1.636	0.724	0.670	1.854	0.095	0.02	4	102	3	160	4	10	2	5
MORB	MORB	unpb	13-12/49f	Atlantic Ocean	Romanche F.Z.	17	89.39	195	80132	1331	293645	2443	1985	141	260	1.661	0.676	0.542	3.048	0.044	0.06	6	478	9	339	11	12	2	8
MORB	MORB	unpb	13-12/49g	Atlantic Ocean	Romanche F.Z.	21	89.23	201	81299	1338	292963	2402	1996	145	262	1.646	0.681	0.554	2.954	0.074	0.06	8	438	8	358	15	15	2	6
MORB	MORB	unpb	13-11/1	Atlantic Ocean	Romanche F.Z.	21	88.11	204	89219	1358	287667	1705	1996	164	307	1.522	0.694	0.619	1.911	0.330	0.01	3	75	2	130	2	9	2	4
MORB	MORB	unpb	13-11/2	Atlantic Ocean	Romanche F.Z.	36	87.44	205	94090	1336	285163	1854	1568	164	341	1.420	0.550	0.517	1.970	0.542	0.05	3	341	6	219	6	11	1	4
MORB	MORB	unpb	13-12/66	Atlantic Ocean	Romanche F.Z.	2	90.56	283	70902	1193	296041	2433	2279	130	356	1.682	0.770	0.546	3.432	-0.001	0.01	13	253	0	1571	18	8	4	7
MORB	MORB	unpb	13-12/78	Atlantic Ocean	Romanche F.Z.	13	89.34	211	79948	1314	291469	2395	2059	147	283	1.643	0.707	0.565	2.996	0.080	0.08	5	562	10	433	18	23	3	9
MORB	MORB	unpb	13-13/5	Atlantic Ocean	Romanche F.Z.	23	89.16	230	81451	1309	291485	1722	1767	161	357	1.607	0.606	0.494	2.114	0.154	0.03	2	238	3	195	3	10	2	2
MORB	MORB	unpb	13-13/14	Atlantic Ocean	Romanche F.Z.	2	88.27	164	87742	1448	287388	1883	1501		284	1.651	0.522	0.458	2.146	0.064	0.08	0	653	0	39	11	8		17
MORB	MORB	(S18)	22-40	Arctic ocean	Knipovich ridge	31	87.56	213	93547	1512	286542	1813	1775	155	288	1.616	0.619	0.579	1.938	0.136	0.04	6	216	4	350	4	35	0	8
MORB	MORB	(S18)	22-23	Arctic ocean	Knipovich ridge	17	87.42	219	94211	1524	284900	1824	1747	157	291	1.618	0.613	0.578	1.936	0.132	0.08	4	406	7	602	6	34		7
WPM-THIN	OIB	(S19)	01-7	Iceland	Reykjanes, Haleyjabunga	52	90.22	344	74156	1176	297683	2335	2518		487	1.586	0.846	0.627	3.148	0.198	0.03	10	252	4	217	11	12		9
WPM-THIN	OIB	(S19)	01-102	Iceland	Reykjanes, Lagafell	31	90.66	355	70780	1142	298921	2440	2520		549	1.614	0.843	0.597	3.447	0.141	0.05	14	362	7	264	17	23		16
WPM-THIN	OIB	(S19)	03-106	Iceland	Reykjanes, Haleyjabunga	65	90.17	337	74317	1175	296602	2308	2498		462	1.581	0.842	0.626	3.105	0.208	0.03	7	197	4	210	10	10		7
WPM-THIN	OIB	(S19)	01-15	Iceland	Reykjanes, Sulur	8	88.39	237	87687	1372	290573	1989	2307		434	1.564	0.794	0.696	2.139	0.243	0.12	8	873	15	681	31	43	2	16
WPM-THIN	OIB	(S19)	01-12	Iceland	Reykjanes, Stapafell	7	87.61	249	92892	1457	285789	1987	2123		368	1.569	0.743	0.690	2.139	0.234	0.13	15	952	15	695	35	73		18
WPM-THIN	OIB	(S19)	01-8	Iceland	Hengill, Midfel	11	90.25	474	73667	1150	296824	2460	2464		671	1.561	0.830	0.612	3.339	0.251	0.10	18	722	9	397	34	39		26
WPM-THIN	OIB	(S19)	01-10	Iceland	Hengill, Midfel	25	89.80	373	76953	1224	294765	2672	2303		543	1.591	0.781	0.601	3.472	0.188	0.05	12	391	5	347	19	30		14
WPM-THIN	OIB	(S19)	01-19	Iceland	Hengill, Maelifell	5	89.24	426	73533	1155	295822	2444	2731	149	643	1.571	0.923	0.679	3.324	0.228	0.19	9	1381	23	719	17	80	6	23
WPM-THIN	OIB	(S19)	03-131	Iceland	Kistufell	67	88.43	295	86728	1335	288535	2170	2305	169	307	1.540	0.799	0.693	2.502	0.294	0.02	9	178	7	196	7	13	1	6
WPM-THIN	OIB	(S19)	03-164	Iceland	Kistufell	25	88.84	331	84046	1287	291132	2174	2411	167	356	1.531	0.828	0.696	2.587	0.311	0.05	10	320	8	429	18	18	2	8

GROUP	Geodynamic setting	References	Sample	Geographic	Locality	N	Fo	Al ppm	Fe ppm	Mn ppm	Mg ppm	Ca ppm	Ni ppm	Co ppm	Cr ppm	100*Mn/Fe	100*Ni/Mg	Ni/(Mg/Fe)/1000	100Ca/Fe	Xpx Mn/Fe	STE Fo wt%	Al ppm	Fe ppm	Mn ppm	Mg ppm	Ca ppm	Ni ppm	Co ppm	Cr ppm
WPM-THIN	OIB	(S19)	03-140	Iceland	Kistufell	45	88.56	305	85843	1311	288225	2161	2359	167	321	1.527	0.816	0.700	2.517	0.320	0.03	9	223	4	186	13	17	1	6
WPM-THIN	OIB	(S19)	03-161	Iceland	Kistufell	50	88.48	286	86408	1326	288657	2157	2341	169	317	1.535	0.811	0.701	2.497	0.303	0.04	10	263	6	215	8	17	1	6
WPM-THIN	OIB	(S19)	01-55	Iceland	Theistareykir,Picrites	24	90.30	356	73313	1168	296901	2439	2489	144	584	1.594	0.838	0.615	3.327	0.182	0.06	19	430	9	356	31	33		21
WPM-THIN	OIB	(S19)	01-57-4	Iceland	Theistareykir,Picrites	32	90.06	379	74874	1187	295369	2371	2467		589	1.586	0.835	0.625	3.167	0.199	0.04	10	288	6	343	22	26	2	15
WPM-THIN	OIB	(S19)	01-56-1	Iceland	Theistareykir,Picrites	48	90.21	299	73806	1189	295885	2435	2423		552	1.611	0.819	0.604	3.299	0.147	0.04	10	284	6	227	15	18		13
WPM-THIN	OIB	(S19)	01-41	Iceland	Theistareykir	15	89.76	437	77047	1178	294013	2177	2800	147	631	1.529	0.952	0.734	2.826	0.316	0.08	17	584	9	406	8	20	2	15
WPM-THIN	OIB	(S19)	01-44	Iceland	Theistareykir	8	89.16	415	81592	1267	292004	2169	2570	155	580	1.553	0.880	0.718	2.658	0.266	0.11	48	803	17	608	76	73	4	53
WPM-THIN	OIB	(S19)	01-56-2	Iceland	Theistareykir,Picrites	9	90.49	350	71973	1149	297838	2425	2491	153	586	1.596	0.836	0.602	3.370	0.177	0.10	30	716	18	414	43	67	3	44
WPM-THIN	OIB	(S19)	01-54	Iceland	Theistareykir,Picrites	45	87.95	293	90335	1407	287024	2183	2297	172	399	1.557	0.800	0.723	2.417	0.258	0.04	7	298	5	226	13	14	1	8
WPM-THIN	OIB	(S19)	01-51	Iceland	Theistareykir,Picrites	6	91.39	367	65650	1035	303239	2433	2287	138	885	1.577	0.754	0.495	3.707	0.217	0.15	38	1176	25	359	108	107	4	71
WPM-THIN	OIB	(S19)	03-224	Iceland	Snaefellsness	4	89.14	292	82132	1272	293273	1994	2363	150	513	1.549	0.806	0.662	2.428	0.275	0.25	12	1823	29	1054	17	86	3	27
WPM-THIN	OIB	(S19)	03-226	Iceland	Snaefellsness	15	88.28	232	88383	1409	289692	2079	1984	161	364	1.594	0.685	0.605	2.352	0.181	0.08	9	580	11	736	69	33	3	16
WPM-THIN	OIB	(S19)	03-220	Iceland	Snaefellsness	5	88.93	245	83462	1344	291820	2073	2067	156	458	1.611	0.708	0.591	2.483	0.147	0.21	23	1484	17	1033	93	55	6	32
WPM-THIN	OIB	(S20)	SM-6	Azores	Sao Migel	26	87.43	166	94610	1469	286286	2062	2067	161	308	1.552	0.596	0.564	2.180	0.268	0.05	2	341	5	243	16	19	2	5
WPM-THIN	OIB	(S20)	SM-10	Azores	Sao Migel	117	88.58	184	85252	1181	287785	1919	2387	151	553	1.385	0.829	0.707	2.251	0.615	0.01	2	78	2	79	6	6	1	3
WPM-THIN	OIB	(S20)	SM-16	Azores	Sao Migel	122	89.18	233	81082	1094	290782	1812	2312	149	672	1.349	0.795	0.645	2.234	0.689	0.02	2	148	3	100	10	26	1	3
WPM-THIN	OIB	(S20)	SM-36a	Azores	Sao Migel	13	89.88	222	75771	1140	292770	1922	2605	139	525	1.504	0.890	0.674	2.537	0.368	0.10	9	761	12	481	26	40	3	13
WPM-THIN	OIB	(S20)	SM-36	Azores	Sao Migel	75	87.91	170	89944	1397	284715	2357	1774	154	355	1.553	0.623	0.560	2.620	0.267	0.03	2	205	4	126	13	8	1	3
WPM-THIN	OIB	(S20)	SM-4	Azores	Sao Migel	4	88.20	177	87865	1297	285844	1887	1925	145	411	1.476	0.674	0.592	2.147	0.425	0.11	3	796	5	465	5	23	5	16
WPM-THIN	OIB	(S20)	SM-33	Azores	Sao Migel	59	88.68	163	84172	1269	287065	2394	2159	149	414	1.508	0.752	0.633	2.844	0.359	0.02	2	175	3	121	17	14	1	3
WPM-THIN	OIB	unpb	T-18	Azores	Terceria	3	88.45	199	86050	1203	286761	1894	2449	152	414	1.398	0.854	0.735	2.201	0.587	0.12	9	838	3	653	98	219	6	44
WPM-THIN	OIB	unpb	T-6	Azores	Terceria	43	88.73	243	84248	1275	288597	1897	2537	144	450	1.513	0.879	0.740	2.251	0.349	0.04	5	277	4	163	14	16	1	7
WPM-THIN	OIB	(S21)	1203a -038R 01W	Pacific Ocean	Detroit smt	57	89.53	344	78587	1160	292482	1837	2987	153	609	1.476	1.021	0.803	2.338	0.426	0.02	7	173	3	182	8	16	1	7
WPM-THIN	OIB	(S21)	1203a -032R	Pacific Ocean	Detroit smt	13	89.73	369	76924	1120	292412	1813	3025	151	628	1.456	1.034	0.796	2.357	0.467	0.07	14	520	9	495	10	32	2	16
WPM-THICK	LIP	(S22)	BR-2	Atlantic Ocean	Mull island	17	87.25	344	96138	1384	286280	2000	2239		445	1.440	0.782	0.752	2.080	0.500	0.07	19	524	9	328	15	35		17
WPM-THICK	LIP	(S22)	BR-5	Atlantic Ocean	Mull island	17	87.99	421	90665	1266	288061	1921	2930		431	1.396	1.014	0.919	2.119	0.592	0.08	11	558	5	423	15	17		12
WPM-THICK	LIP	(S22)	BR-6	Atlantic Ocean	Mull island	11	87.83	435	91782	1322	288114	1982	2459		552	1.441	0.854	0.783	2.159	0.499	0.12	17	904	14	376	8	28		16
WPM-THICK	LIP	(S22)	BHL-15	Atlantic Ocean	Mull island	33	88.24	404	89264	1333	291557	2119	2386		510	1.493	0.818	0.730	2.374	0.391	0.04	7	326	5	230	3	17		7
WPM-THICK	LIP	(S22)	BHL-19	Atlantic Ocean	Mull island	16	87.83	463	92074	1353	289015	2151	2562		567	1.469	0.887	0.816	2.336	0.440	0.07	21	557	11	305	31	72		22
WPM-THICK	LIP	(S22)	BHL-34	Atlantic Ocean	Mull island	24	87.77	410	92639	1335	289280	2043	2655		476	1.441	0.918	0.850	2.205	0.499	0.05	19	396	6	259	5	22		13
WPM-THICK	LIP	(S22)	BCH-14	Atlantic Ocean	Mull island	10	86.50	461	101517	1375	282942	2043	2701		411	1.355	0.955	0.969	1.875	0.677	0.12	19	875	12	594	9	32		16
WPM-THICK	LIP	(S22)	BCH-24	Atlantic Ocean	Mull island	14	89.35	437	80685	1195	300460	2042	2912		654	1.482	0.989	0.798	2.533	0.414	0.09	6	688	11	495	16	28		14
WPM-THICK	LIP	(S22)	BCH-27	Atlantic Ocean	Mull island	24	88.90	426	84083	1233	292930	1958	2849		626	1.466	0.973	0.818	2.428	0.446	0.06	8	423	6	267	8	8		7
WPM-THICK	LIP	(S22)	BCH-33	Atlantic Ocean	Mull island	20	88.38	419	87922	1262	290969	1956	2782		550	1.435	0.956	0.841	2.227	0.510	0.06	10	434	7	295	7	16		9
WPM-THICK	LIP	(S22)	AM-7a	Atlantic Ocean	Mull island	18	86.21	407	102948	1438	280159	2151	2396		328	1.397	0.855	0.880	1.900	0.590	0.06	7	430	7	303	20	18		11
WPM-THICK	LIP	(S22)	BB-22	Atlantic Ocean	Mull island	12	86.68	319	99731	1345	282319	1621	2549		385	1.349	0.903	0.900	1.626	0.690	0.12	21	785	11	654	31	63		32
WPM-THICK	LIP	(S22)	B-26	Atlantic Ocean	Mull island	3	86.66	450	99990	1417	282639	2101	2606		481	1.417	0.922	0.922	2.101	0.547	0.31	53	2177	19	1420	121	97		75
WPM-THICK	LIP	(S22)	B-29	Atlantic Ocean	Mull island	12	87.29	393	95617	1355	285840	1955	2696		448	1.417	0.943	0.902	2.044	0.547	0.09	52	613	39	532	33	23		15
WPM-THICK	LIP	(S23)	BB	Atlantic Ocean	Baffin Bay	1	92.65	386	55709	898	305505	2051	3450	118	828	1.613	1.129	0.629	3.682	0.143	0.00	14	564	6	391	12	9	2	14
WPM-THICK	LIP	(S24)	95976	Atlantic Ocean	Greenland	16	92.05	487	68080	944	304500	1894	3749	125	886	1.562	1.231	0.745	3.132	0.249	0.08	14	390	4	286	11	14	1	16
WPM-THICK	LIP	(S24)	27141	Atlantic Ocean	Greenland	32	90.93	469	68080	1032	296916	1944	3499	136	848	1.515	1.178	0.802	2.856	0.344	0.05	8	500	7	277	16	24	2	12
WPM-THICK	LIP	(S24)	G-27142	Atlantic Ocean	Greenland	21	91.06	310	67782	1062	300460	1872	3128	143	551	1.567	1.041	0.706	2.762	0.236	0.07	6	217	3	142	8	6	1	5
WPM-THICK	LIP	unpb	Dis-1	Atlantic Ocean	Disko	75	88.50	310	86270	1329	288974	2028	3006		468	1.541	1.040	0.897	2.350	0.292	0.03	3	157	3	124	6	7	1	3
WPM-THICK*	LIP	(S10)	1185A 9R 2 92-96	Pacific Ocean	Ontong Java Plateau	80	87.36	250	94242	1463	283514	2121	2156	167	377	1.553	0.760	0.717	2.250	0.267	0.02	6	604	8	362	15	48	3	30
WPM-THICK*	LIP	(S10)	1187A 10R 7 46-49	Pacific Ocean	Ontong Java Plateau	15	88.76	269	83907	1115	288325	1584	3313	152	743	1.328	1.149	0.964	1.887	0.731	0.08	25	377	7	704	32	70	3	41
WPM-THICK*	LIP	(S10)	1187A 6R 6 116-119	Pacific Ocean	Ontong Java Plateau	4	89.33	292	79928	1202	291333	1910	2448	157	506	1.504	0.840	0.672	2.390	0.367	0.07	8	491	7	339	11	44	2	31
WPM-THICK	LIP	(S25)	P23-9	Africa	Karoo	21	88.28	361	87816	1245	287906	1632	2681	155	836	1.439	0.818	0.761	1.848	0.527	0.04	7	303	4	240	9	11	2	24
WPM-THICK	LIP	(S25)	P23-32	Africa	Karoo	25	89.49	124	79080	1138	293022	1632	2822	149	1106	1.417	0.963	0.761	2.063	0.484	0.05	4	390	5	276	9	9	1	11
WPM-THICK	LIP	(S25)	N356	Africa	Karoo	29	90.42	256	72082	922	296170	1084	4392		486	1.279	1.483	1.069	1.504	0.835	0.05	14	284	5	301	39	18		19
WPM-THICK	LIP	(S26)	EM-43	China	Emeishan	26	90.47	213	72181	1286	298304	2612	2566	155	470	1.781	0.860	0.621	3.619	-0.207	0.04	14	390	5	286	13	24	1	19
WPM-THICK	LIP	(S27)	EM-55	China	Emeishan	5	90.59	213	71310	1036	298830	2084	3418		551	1.453	1.144	0.816	2.922	0.473	0.26	27	1869	29	1261	163	80	1	24
WPM-THICK	LIP	(S27)	EM-57	China	Emeishan	4	90.69	208	71013	1020	301066	1728	3399		487	1.437	1.129	0.802	2.433	0.507	0.40	41	3014	38	1492	24	51		51
WPM-THICK	LIP	(S27)	EM-58	China	Emeishan	4	90.76	208	69952	1001	298979	1796	3548		523	1.431	1.187	0.830	2.567	0.519	0.35	22	2640	36	1104	186	143		60
WPM-THICK	LIP	unpb	4270	Siberia, Norilsk	Gudchikhinskaya unit	15	79.90	170	146601	1770	253513	1914	2942		299	1.207	1.161	1.702	1.306	0.982	0.09	3	601	9	371	8	28		7
WPM-THICK	LIP	unpb	XC51-130	Siberia, Norilsk	Gudchikhinskaya unit	7	82.41	160	128631	1619	262206	1698	3016		379	1.258	1.150	1.480	1.320	0.877	0.16	6	1071	18	660	25	24		12
WPM-THICK	LIP	unpb	XC51-130(n)	Siberia, Norilsk	Gudchikhinskaya unit	7	82.74	130	126790	1582	264503	1805	3102	200	383	1.247	1.173	1.487	1.424	0.899	0.10	5	747	11	466	12	18	2	19

GROUP	Geodynamic setting	References	Sample	Geographic	Locality	N	Fo	Al ppm	Fe ppm	Mn ppm	Mg ppm	Ca ppm	Ni ppm	Co ppm	Cr ppm	100*Mn/Fe	100*Ni/Mg	Ni/(Mg/Fe)/1000	100Ca/Fe	X px Mn/Fe	STE	Fo wt%	Al ppm	Fe ppm	Mn ppm	Mg ppm	Ca ppm	Ni ppm	Co ppm	Cr ppm
WPM-THICK	LIP	unpb	SU-50	Siberia, Norilsk	Gudchikhinskaya unit	22	80.80	163	140093	1691	256505	1930	3017		327	1.207	1.176	1.648	1.378	0.983		0.07	3	501	6	341	7	19		6
WPM-THICK	LIP	(S28)	AK-31	Africa, Afar	Zawl-Kelkelti, Emba Tekera, Eritrea	5	87.10	374	96459	1382	283503	1933	2112	169	371	1.432	0.745	0.719	2.003	0.516		0.16	31	1149	17	711	16	58	2	22
WPM-THICK	LIP	(S28)	AK-33	Africa, Afar	Zawl-Kelkelti, Emba Tekera, Eritrea	9	89.34	475	79972	1186	291758	1891	2712	158	480	1.483	0.929	0.743	2.364	0.412		0.10	17	711	9	421	8	26	3	12
WPM-THICK	LIP	(S28)	AG-10	Africa, Afar	Adi Ghebray, Emba Tekera, Eritrea	1	88.30	513	87011	1286	285738	1908	2562	154	493	1.477	0.897	0.780	2.193	0.423		0.00								
WPM-THICK	LIP	(S28)	AG-15	Africa, Afar	Adi Ghebray, Emba Tekera, Eritrea	17	84.66	358	112774	1530	270733	1997	2154	182	295	1.356	0.795	0.897	1.546	0.673		0.07	8	483	8	259	8	35	3	15
WPM-THICK	OIB	(S29)	RY-7	Indian Ocean	Reunion, Piton de Neige	73	85.86	224	105445	1567	278606	1675	2377		329	1.486	0.853	0.900	1.894	0.405		0.02	3	149	3	104	11	5		3
WPM-THICK	OIB	(S29)	RY-11	Indian Ocean	Reunion, Piton de Neige	13	89.82	262	77028	1125	295786	1988	2970		534	1.460	1.004	0.774	2.174	0.459		0.08	9	545	11	444	28	38		12
WPM-THICK	OIB	(S29)	OPF	Indian Ocean	Reunion, Piton de la Fournaise	82	83.98	185	118585	1696	270479	1780	2016		243	1.430	0.745	0.884	1.677	0.521		0.03	2	186	3	104	5	3		2
WPM-THICK	OIB	unpb	IKI-22	Hawaii	Kilauea Iki	8	88.28	255	87957	1205	288325	1742	3059	161	600	1.370	1.061	0.933	2.023	0.645		0.13	16	957	12	441	10	49	3	17
WPM-THICK	OIB	unpb	IKI-44	Hawaii	Kilauea Iki	20	88.54	288	85808	1176	288577	1868	3210	158	614	1.371	1.112	0.954	2.030	0.643		0.05	4	368	5	319	12	33	2	6
WPM-THICK	OIB	unpb	K97-12	Hawaii	Kilauea Iki	34	87.81	236	91085	1259	285538	1376	2915	159	544	1.382	1.021	0.930	2.050	0.621		0.05	6	365	6	207	20	17	1	7
WPM-THICK	OIB	unpb	K97-14b	Hawaii	Mouna Loa, Puu Wahi	67	88.41	255	86630	1195	287459	1352	3023	161	607	1.379	1.051	0.911	1.589	0.627		0.03	154	4	220	7	14	1	7	247
WPM-THICK	OIB	(S30)	SR-17-9.0	Hawaii	Mauna Loa, HSDP-2	31	90.22	264	73484	998	294988	1359	3300	165	663	1.357	1.119	0.822	1.840	0.671		0.02	2	134	2	131	2	26	1	15
WPM-THICK	OIB	(S30)	SR-18-0	Hawaii	Mauna Loa, HSDP-2	19	90.53	257	71919	994	299311	1791	3918		692	1.382	1.309	0.941	1.889	0.620		0.08	11	578	8	279	6	37		27
WPM-THICK	OIB	(S30)	SR-31-1.0-2.0	Hawaii	Mauna Loa, HSDP-2	7	89.32	196	81356	1133	295986	1428	2883		584	1.393	0.974	0.792	2.201	0.599		0.13	18	932	20	675	118	143		14
WPM-THICK	OIB	(S30)	SR-98-2.5-3.0	Hawaii	Mauna Loa, HSDP-2	31	88.94	278	76622	1031	297952	1398	3928	151	710	1.346	1.318	1.010	1.863	0.695		0.05	7	394	5	275	6	49	1	18
WPM-THICK	OIB	(S30)	SR-98-2.5-3.0(n)	Hawaii	Mauna Loa, HSDP-2	60	89.75	299	76967	1045	293323	1385	3830	150	736	1.358	1.306	1.005	1.817	0.670		0.02	4	172	3	165	7	26	1	11
WPM-THICK	OIB	(S30)	SR-101-7.0	Hawaii	Mauna Loa, HSDP-2	50	90.00	318	74911	1035	293507	1405	3727		784	1.382	1.270	0.951	1.849	0.621		0.03	2	188	3	125	3	24		6
WPM-THICK	OIB	(S30)	SR-104-5.5	Hawaii	Mauna Loa, HSDP-2	33	89.89	276	77006	1054	297965	1413	3700		745	1.368	1.242	0.956	1.824	0.649		0.05	3	387	6	217	3	21		9
WPM-THICK	OIB	(S30)	SR-104-5.5(n)	Hawaii	Mauna Loa, HSDP-2	70	89.77	276	77197	1057	294744	1409	3729	144	735	1.370	1.265	0.977	1.830	0.646		0.03	3	203	3	149	3	13	1	8
WPM-THICK	OIB	(S30)	SR-113-6.5	Hawaii	Mauna Loa, HSDP-2	63	89.58	273	77943	1057	291517	1397	3702		568	1.357	1.270	0.990	1.808	0.673		0.03	3	210	3	153	2	10		5
WPM-THICK	OIB	(S30)	SR-117-4.0	Hawaii	Mauna Loa, HSDP-2	13	89.67	305	76422	1046	288664	1429	3680		836	1.368	1.275	0.974	1.828	0.649		0.11	10	782	8	373	6	39		15
WPM-THICK	OIB	(S30)	SR-120-2.0-2.5	Hawaii	Mauna Loa, HSDP2	35	89.65	258	78973	1075	297548	1453	3632		732	1.361	1.221	0.964	1.809	0.664		0.04	6	296	5	203	4	22		8
WPM-THICK	OIB	(S30)	SR-120-2.0-2.5(n)	Hawaii	Mauna Loa, HSDP2	40	89.30	275	80462	1085	292328	2011	3565	150		1.349	1.220	0.981	1.806	0.689		0.04	9	305	5	197	4	19	1	0
WPM-THICK	OIB	(S30)	SR-133-10.0	Hawaii	Mauna Loa, HSDP2	7	87.33	211	95193	1310	285497	1537	2815		428	1.376	0.986	0.939	2.113	0.633		0.13	9	942	11	649	23	70		12
WPM-THICK	OIB	(S30)	SR-134-2.6	Hawaii	Mauna Loa, HSDP2	25	86.71	212	98879	1354	280742	1531	2725	172	406	1.370	0.971	0.960	2.089	0.646		0.06	6	397	6	270	21	13	2	9
WPM-THICK	OIB	(S30)	SR-136-6.1	Hawaii	Mauna Kea, HSDP2	16	89.20	210	82042	1101	294758	1666	3140		630	1.342	1.065	0.874	1.873	0.703		0.08	6	550	8	426	9	63		12
WPM-THICK	OIB	(S30)	SR-138-6.5	Hawaii	Mauna Kea, HSDP2	31	89.28	263	80686	1096	292513	1719	3197	157	667	1.359	1.093	0.882	1.898	0.668		0.05	5	347	6	206	10	33	1	8
WPM-THICK	OIB	(S30)	SR-139-9.5	Hawaii	Mauna Kea, HSDP2	39	89.05	243	82338	1125	291274	1728	3077		698	1.366	1.056	0.870	2.024	0.653		0.05	5	349	6	253	10	22		6
WPM-THICK	OIB	(S30)	SR-144-2.0	Hawaii	Mauna Kea, HSDP2	23	88.58	168	86738	1181	292769	1877	2961		464	1.361	1.012	0.877	1.982	0.664		0.07	5	470	8	323	20	20		14
WPM-THICK	OIB	(S30)	SR-145-2.5-2.6	Hawaii	Mauna Kea, HSDP2	39	88.55	201	86149	1170	292005	1908	2962		656	1.359	1.021	0.880	2.005	0.669		0.05	4	340	5	189	5	11		13
WPM-THICK	OIB	(S30)	SR-148-8.5	Hawaii	Mauna Kea, HSDP2	19	88.00	201	90074	1241	287469	1877	2679	164	552	1.377	0.932	0.839	2.083	0.630		0.08	7	561	9	385	29	21	1	7
WPM-THICK	OIB	(S30)	SR-149-1.0	Hawaii	Mauna Kea, HSDP2	31	87.92	190	91454	1258	289528	1908	2655		548	1.375	0.917	0.839	2.086	0.634		0.06	8	414	7	267	14	19		13
WPM-THICK	OIB	(S30)	SR-157-6.1	Hawaii	Mauna Kea, HSDP2	24	89.11	196	82064	1126	292116	1640	3079		596	1.372	1.054	0.865	1.999	0.641		0.06	4	423	7	272	21	23		7
WPM-THICK	OIB	(S30)	SR-159-2.6	Hawaii	Mauna Kea, HSDP2	42	88.75	244	84807	1154	291029	1648	3036	159	643	1.360	1.043	0.885	1.943	0.665		0.04	8	288	3	211	9	14		8
WPM-THICK	OIB	(S30)	SR-170-1.2	Hawaii	Mauna Kea, HSDP2	19	88.30	213	88271	1193	289785	1746	2940		627	1.351	1.014	0.895	1.867	0.685		0.07	8	530	8	347	10	40		16
WPM-THICK	OIB	(S30)	SR-170-3.1	Hawaii	Mauna Kea, HSDP2	46	87.98	218	89822	1217	286190	1668	2933		629	1.355	1.025	0.921	1.857	0.677		0.04	5	282	4	185	11	16		7
WPM-THICK	OIB	(S30)	SR-175-5.2	Hawaii	Mauna Kea, HSDP2	42	89.02	241	83748	1123	293387	1546	3210		696	1.340	1.094	0.916	1.845	0.707		0.05	4	352	6	214	16	26		11
WPM-THICK	OIB	(S30)	SR-184-3.0	Hawaii	Mauna Kea, HSDP2	36	88.95	201	80222	1115	293005	1746	3096	165	513	1.390	1.057	0.848	2.176	0.604		0.29	10	2119	9	1187	81	8	6	9
WPM-THICK	OIB	(S30)	SR-188-6.5	Hawaii	Mauna Kea, HSDP2	4	89.35	240	78725	1053	293534	1541	3340	152	556	1.338	1.138	0.896	1.958	0.712		0.15	10	1109	25	654	48	213	6	30
WPM-THICK	OIB	(S30)	SR-260-8.5	Hawaii	Mauna Kea, HSDP2	6	89.55	257	77396	1004	294114	1434	3847	134	590	1.297	1.308	1.012	1.852	0.797		0.13	11	980	11	567	14	53	6	14
WPM-THICK	OIB	(S30)	SR-277-7.5-8.0	Hawaii	Mauna Kea, HSDP2	2	90.86	267	69347	906	299834	1361	3693	146	380	1.307	1.232	0.854	1.963	0.777		0.14	13	999	0	709	11	55	1	38
WPM-THICK	OIB	(S30)	SR-291-3.0-3.8	Hawaii	Mauna Kea, HSDP2	38	89.24	201	81114	1115	292628	1645	3327	149	603	1.374	1.137	0.922	2.028	0.637		0.04	7	316	4	210	12	18	1	12
WPM-THICK	OIB	(S30)	SR-298-6.0	Hawaii	Mauna Kea, HSDP2	27	89.03	247	82446	1102	291201	1575	3328	149	664	1.337	1.143	0.942	1.910	0.715		0.06	6	424	8	236	10	49	2	11
WPM-THICK	OIB	(S30)	SR-308-0-0.6	Hawaii	Mauna Kea, HSDP2	12	89.10	277	81993	1099	291738	1557	3478	151	639	1.340	1.192	0.977	1.899	0.707		0.13	8	952	17	611	26	108	3	8
WPM-THICK	OIB	(S30)	SR-310-2.4-2.8	Hawaii	Mauna Kea, HSDP2	70	89.51	265	79437	1082	294797	1548	3305	153	742	1.362	1.121	0.891	1.949	0.662		0.03	3	192	3	130	2	14	1	5
WPM-THICK	OIB	(S30)	SR-319-7.5	Hawaii	Mauna Kea, HSDP2	42	89.02	218	82543	1097	291302	1551	3384	153	680	1.329	1.162	0.959	1.879	0.730		0.04	5	316	5	202	15	26	1	10
WPM-THICK	OIB	(S30)	SR-332-9.8-10.0	Hawaii	Mauna Kea, HSDP2	7	90.31	222	73336	981	297371	1476	4121	137	487	1.338	1.386	1.016	2.013	0.711		0.14	9	1015	15	623	15	112	2	21
WPM-THICK	OIB	(S30)	SR-335-3.2-3.4	Hawaii	Mauna Kea, HSDP2	55	89.89	286	75966	1037	293764	1500	3345	149	785	1.365	1.139	0.865	1.975	0.656		0.04	4	268	4	201	4	25	1	9
WPM-THICK	OIB	(S30)	SR-337-3.4-3.7	Hawaii	Mauna Kea, HSDP2	58	89.78	265	76896	1041	294088	1504	3344	150	740	1.354	1.137	0.874	1.956	0.678		0.04	6	318	4	187	6	25	1	10
WPM-THICK	OIB	(S30)	SR-353-7.2-7.4	Hawaii	Mauna Kea, HSDP2	62	88.01	229	89908	1210	287179	1660	3108	146	553	1.345	1.082	0.973	1.846	0.697		0.03	5	236	3	177	9	22	1	6
WPM-THICK	OIB	(S30)	SR-361-5-2.8	Hawaii	Mauna Kea, HSDP2	26	89.66	231	77985	1050	294211	1498	3512	148	602	1.346	1.194	0.931	1.921	0.695		0.04	5	286	4	173	5	12	1	11
WPM-THICK	OIB	(S30)	SR-363-7.0-8.0	Hawaii	Mauna Kea, HSDP2	57	89.03	228	82751	1107	292365	1584	3346	151	603	1.337	1.144	0.947	1.914	0.713		0.03	6	226	4	155	4	14	1	13
WPM-THICK	OIB	(S30)	SR-375-0.5-1.0	Hawaii	Mauna Kea, HSDP2	20	89.65	243	78027	1048	294222	1534	3468	146	738	1.343	1.179	0.920	1.967	0.702		0.06	8	444	6	244	6	32	1	11
WPM-THICK	OIB	(S30)	SR-377-6.7-6.9	Hawaii	Mauna Kea, HSDP2	38	89.36	276	79989	1060	292396	1534	3617	146	731	1.325	1.237	0.990	1.918	0.739		0.04	5	257	3	210	11	8	1	11
WPM-THICK	OIB	(S30)	SR-382-4.0-4.4	Hawaii	Mauna Kea, HSDP2		88.26	238	87648	1166	286814	1619	3256	156	660	1.330	1.135	0.995	1.847	0.728		0.08	11	561	8	320	9	28	2	24

S7

GROUP	Geodynamic setting	References	Sample	Locality	Geographic	N	Fo	Al ppm	Fe ppm	Mn ppm	Mg ppm	Ca ppm	Ni ppm	Co ppm	Cr ppm	100*Mn/Fe	100*Ni/Mg	Ni/(Mg/Fe)/1000	100Ca/Fe	X px Mn/Fe	STE	Fo wt%	Al ppm	Fe ppm	Mn ppm	Mg ppm	Ca ppm	Ni ppm	Co ppm	Cr ppm
WPM-THICK	OIB	(S30)	SR-389-1.8-2.0	Mauna Kea, HSDP2	Hawaii	35	89.76	303	77207	1041	294410	1505	3425	147	795	1.349	1.163	0.898	1.949	0.690		0.04	2	297	4	232	3	42	2	11
WPM-THICK	OIB	(S30)	SR-565-0.7	Mauna Kea, HSDP2	Hawaii	4	90.28	287	73350	962	296380	1261	4117	149	547	1.312	1.389	1.019	1.720	0.766		0.01	8	205	5	610	12	12	6	3
WPM-THICK	OIB	(S30)	SR-882.9.8-10	Mauna Kea, HSDP2	Hawaii	50	88.70	289	84690	1138	289380	1576	3212	158	723	1.343	1.110	0.940	1.861	0.701		0.03	4	242	4	163	6	17	1	5
WPM-THICK	OIB	(S30)	SR-684-5.0-5.5	Mauna Kea, HSDP2	Hawaii	28	88.91	284	83330	1111	290795	1550	3209	161	731	1.333	1.103	0.920	1.860	0.723		0.04	4	274	4	184	6	31	2	8
WPM-THICK	OIB	(S30)	SR-690-4.0	Mauna Kea, HSDP2	Hawaii	16	89.67	307	77869	1032	294148	1587	3651	150	723	1.325	1.241	0.967	2.038	0.738		0.08	4	622	5	293	10	18	3	10
WPM-THICK	OIB	(S30)	SR-694-3.0-3.2	Mauna Kea, HSDP2	Hawaii	2	89.01	278	82822	1104	292028	1601	3544	157	770	1.332	1.214	1.005	1.933	0.723		0.07	13	428	4	525	7	63	6	65
WPM-THICK	OIB	(S30)	SR-930-9.1	Mauna Kea, HSDP2	Hawaii	10	89.28	276	80768	1122	292698	1545	3395	155	695	1.389	1.160	0.937	1.913	0.605		0.10	9	746	10	575	27	85	3	27
WPM-THICK	OIB	(S30)	SR-942-5.7	Mauna Kea, HSDP2	Hawaii	40	88.14	229	88920	1206	287592	1468	3102	164	601	1.356	1.079	0.959	1.651	0.674		0.04	5	267	4	190	7	10	2	8
WPM-THICK	OIB	(S30)	SR-954-10.7	Mauna Kea, HSDP2	Hawaii	48	89.52	289	78227	1059	290821	1487	3631	147	779	1.353	1.249	0.977	1.900	0.680		0.03	4	212	3	153	2	13	1	5
WPM-THICK	OIB	(S30)	SR-961-14.0	Mauna Kea, HSDP2	Hawaii	44	89.44	261	79445	1082	292711	1506	3537		765	1.362	1.208	0.960	1.895	0.662		0.04	4	311	3	195	3	29		7
WPM-THICK	OIB	(S30)	SR-962-18.1	Mauna Kea, HSDP2	Hawaii	66	89.51	284	79029	1075	293375	1488	3580	152	773	1.361	1.220	0.964	1.882	0.665		0.03	4	208	3	147	3	15	1	5
WPM-THICK	OIB	(S31)	KI-11	Mauna Kea, post shield	Hawaii	18	86.98	132	98166	1423	285490	2424	2233		366	1.450	0.782	0.768	2.470	0.480		0.07	6	472	8	309	20	14		9
WPM-THICK	OIB	(S31)	KI-8	Mauna Kea post shield	Hawaii	9	88.26	181	89202	1229	291934	1832	2448		536	1.378	0.839	0.748	2.054	0.630		0.12	8	818	14	604	30	60		10
WPM-THICK	OIB	(S31)	KI-4	Mauna Kea post shield	Hawaii	11	87.74	139	92943	1295	289526	2043	2588		446	1.393	0.894	0.831	2.198	0.598		0.11	5	791	11	499	68	30		18
WPM-THICK	OIB	(S31)	KI-3	Mauna Kea post shield	Hawaii	8	88.79	251	84979	1150	292785	1590	2916		654	1.353	0.996	0.846	1.871	0.680		0.12	11	901	17	595	29	100		13
WPM-THICK	OIB	(S31)	KI-3(n)	Mauna Kea, post shield	Hawaii	5	88.82	234	84025	1145	290374	1562	2951	159	642	1.362	1.016	0.854	1.859	0.661		0.21	11	1510	28	1002	68	134	3	20
WPM-THICK	OIB	(S32)	Koo-10	Koolau, Makapuu	Hawaii	7	87.13	179	96799	1263	285148	1274	2967		479	1.305	1.040	1.007	1.316	0.780		0.14	7	1030	10	495	8	24		8
WPM-THICK	OIB	(S32)	Koo-17a	Koolau, Makapuu	Hawaii	19	89.11	241	82175	1085	292709	1199	3910		613	1.321	1.336	1.098	1.459	0.747		0.08	6	541	11	417	13	98		12
WPM-THICK	OIB	(S32)	Koo-19a	Koolau, Makapuu	Hawaii	43	88.82	248	84276	1111	291260	1257	3707		610	1.318	1.273	1.073	1.492	0.753		0.04	6	275	5	170	8	36		6
WPM-THICK	OIB	(S32)	Koo-30a	Koolau, Makapuu	Hawaii	2	86.74	180	99604	1348	283591	1354	3505		404	1.353	1.236	1.231	1.360	0.681		0.04	11	459	8	362	32	47		21
WPM-THICK	OIB	(S32)	Koo-49	Koolau, Makapuu	Hawaii	34	89.00	235	83005	1096	292194	1272	3803		579	1.320	1.302	1.080	1.532	0.748		0.03	5	227	6	212	7	37		10
WPM-THICK	OIB	(S32)	Koo-55	Koolau, Makapuu	Hawaii	41	88.52	215	87012	1156	292015	1294	3584		557	1.329	1.227	1.068	1.488	0.731		0.03	5	213	4	165	6	18		7
WPM-THICK	OIB	unpb	S10(i)	Koolau, Makapuu	Hawaii	23	86.78	194	96745	1289	281959	1239	3129	171	475	1.306	1.110	1.096	1.254	0.751		0.04	3	307	5	213	6	35	1	6
WPM-THICK	OIB	unpb	S10(ii)	Koolau, Makapuu	Hawaii	23	87.86	230	90851	1142	286085	1194	4503	169	482	1.257	1.574	1.430	1.314	0.879		0.35	3	2433	12	1667	21	149	5	24
WPM-THICK	OIB	(S33)	R8-1.1-1197.1	Koolau, KSDP	Hawaii	23	88.67	248	85157	1136	288945	1366	3516	152	620	1.334	1.213	1.033	1.604	0.720		0.04	7	299	5	323	14	49	2	7
WPM-THICK	OIB	(S34)	LO-02-04	Loihi smt	Hawaii	28	88.70	236	91993	1283	285314	1984	2753		528	1.394	0.965	0.888	2.156	0.595		0.05	7	395	7	248	22	29		10
WPM-THICK	OIB	(S34)	LO-02-02	Loihi smt	Hawaii	19	88.29	219	88152	1233	289083	2036	2811		542	1.399	0.972	0.857	2.309	0.585		0.07	5	515	8	282	66	35		17
WPM-THICK	OIB	(S35)	158-9	Loihi smt	Hawaii	44	89.15	239	81977	1166	292971	1781	3100		659	1.423	1.058	0.867	2.172	0.536		0.03	5	193	3	131	15	12		6
WPM-THICK	OIB	(S35)	186-5	Loihi smt	Hawaii	3	89.43	309	78637	1131	293326	2015	2879		712	1.420	0.981	0.782	2.531	0.542		0.34	14	2415	45	1594	84	123		51
WPM-THICK	OIB	(S35)	187-1	Loihi smt	Hawaii	7	89.67	303	78190	1095	295195	1774	3242		679	1.401	1.098	0.859	2.269	0.582		0.12	16	898	14	488	36	121		29
WPM-THICK	OIB	(S36)	M2343-7	Loihi smt	Hawaii	9	88.14	215	89237	1319	288692	1899	2742		483	1.478	0.950	0.848	2.459	0.421		0.13	17	973	14	586	26	11		12
WPM-THICK	OIB	(S36)	M2335-12	Loihi smt	Hawaii	13	88.21	258	88346	1221	287678	2180	2962		683	1.382	1.030	0.839	2.365	0.516		0.08	11	619	11	378	28	28		23
WPM-THICK	OIB	(S36)	M2340-3	Loihi smt	Hawaii	3	87.11	222	96131	1351	282756	1826	2823		511	1.405	0.998	0.987	2.041	0.573		0.32	26	2393	37	1203	88	156		39
WPM-THICK	OIB	(S36)	M2343-10	Loihi smt	Hawaii	23	89.44	210	96726	1291	283961	1911	3023		350	1.404	1.054	0.941	2.367	0.628		0.03	5	186	4	157	11	8		8
WPM-THICK	OIB	(S36)	M2343-8	Loihi smt	Hawaii	37	87.56	217	83863	1242	283538	2272	2781		434	1.481	0.981	0.865	2.450	0.500		0.13	37	914	11	569	51	9		36
WPM-THICK	OIB	(S36)	M2340-1	Loihi smt	Hawaii	3	87.16	220	95978	1382	288238	2180	2804		620	1.440	0.973	0.910	2.149	0.468		0.17	40	1340	14	269	43	99		28
WPM-THICK	OIB	(S36)	MC2337-4	Loihi smt	Hawaii	5	86.86	211	98509	1385	286500	1996	2714		468	1.456	0.947	0.936	2.135	0.608		0.06	10	524	12	364	43	28		11
WPM-THICK	OIB	(S36)	M2343-9	Loihi smt	Hawaii	21	87.57	235	93496	1298	289233	2311	3149		445	1.382	1.085	0.843	2.679	0.553		0.19	12	1356	27	891	64	40		10
WPM-THICK	OIB	(S36)	M2343-5	Loihi smt	Hawaii	5	88.54	207	86290	1221	283074	2372	3074		504	1.414	1.029	0.883	2.483	0.516		0.18	20	1341	16	790	66	36		30
WPM-THICK	OIB	(S36)	M2336-5	Loihi smt	Hawaii	6	87.20	200	95500	1368	292960	1962	3015		385	1.433	1.010	0.820	2.463	0.511		0.06	7	391	9	379	35	56		14
WPM-THICK	OIB	(S36)	M2336-4	Loihi smt	Hawaii	22	89.42	232	79649	1143	284070	2341	2870		534	1.435	0.870	0.950	2.489	0.546		0.19	4	1438	27	659	49	72		19
WPM-THICK	OIB	(S36)	M2338-5	Loihi smt	Hawaii	5	87.41	196	94048	1334	280346	2559	2438		423	1.418	0.896	0.896	2.483	0.545		0.06	5	420	8	280	39	61		11
WPM-THICK	OIB	(S36)	M2336-7	Loihi smt	Hawaii	5	86.21	192	103052	1462	286982	2045	2715		298	1.419	0.946	0.857	2.258	0.432		0.09	12	674	12	429	123	42		25
WPM-THICK	OIB	(S36)	M2335-R	Loihi smt	Hawaii	13	87.93	207	90549	1334	286031	1352	3547		428	1.473	1.240	1.087	1.542	0.644		0.17	8	1214	18	775	44	71	4	15
WPM-THICK	OIB	unpb	5328	Kauai-Haena	Hawaii	1	88.92	259	83039	1046	288996	1401	3874		554	1.259	1.336	1.109	1.687	0.875		0.00	0	0	0	0	0	0	0	0
WPM-THICK	OIB	unpb	0433c-033R	Suiko smt	Pacific Ocean	11	88.46	326	86371	1156	287978	1559	3370	162	655	1.338	1.170	1.011	1.805	0.711		0.08	9	610	9	530	21	19	2	13
WPM-THICK	OIB	unpb	0433c-024R	Suiko smt	Pacific Ocean	21	88.77	280	89054	1294	279860	1627	2943	174	552	1.319	1.051	1.031	1.659	0.750		0.06	7	460	7	317	12	37	3	12
WPM-THICK	OIB	(S37)	LG-99-58	La Gomera	Atlantic Ocean	5	89.13	252	91918	1209	292195	1905	2839	155	477	1.476	0.972	0.796	2.326	0.425		0.10	5	712	6	557	46	160	3	12
WPM-THICK	OIB	(S37)	GC-98-59	Gran Canaria	Atlantic Ocean	5	89.46	221	79780	1182	294670	1711	3046	153	464	1.481	1.034	0.825	2.144	0.415		0.14	5	871	7	1514	74	96	6	15
WPM-THICK	OIB	(S37)	GC-98-35	Gran Canaria	Atlantic Ocean	3	89.21	180	81152	1196	291839	1753	2997	153	434	1.474	1.027	0.833	2.161	0.430		0.16	8	1022	23	1094	60	209	4	6
WPM-THICK	OIB	(S37)	GC-1265	Gran Canaria	Atlantic Ocean	5	89.56	171	78629	1219	293671	2085	2705	152	367	1.551	0.921	0.724	2.652	0.271		0.23	19	1481	21	1705	81	45	1	37
WPM-THICK	OIB	(S38)	953C-101R-5 116-123	Gran Canaria	Atlantic Ocean	13	88.23	197	87674	1202	286031	1352	3547	154	486	1.371	1.240	1.087	1.542	0.644		0.17	8	1214	18	775	44	71	4	13
WPM-THICK	OIB	(S38)	953O-90R-05 13-21	Gran Canaria	Atlantic Ocean	14	88.67	222	84795	1161	288663	1447	3471	152	518	1.369	1.203	1.020	1.706	0.648		0.08	3	555	8	335	6	39	3	10

Sobolev et al, Supporting Online Material www.sciencemag.org/cgi/content/full/1138113/DC1

GROUP	Geodynamic setting	References	Sample	Geographic	Locality	N	Fo	Al ppm	Fe ppm	Mn ppm	Mg ppm	Ca ppm	Ni ppm	Co ppm	Cr ppm	100*Mn/Fe	100*Ni/Mg	Ni/(Mg/Fe)/1000	100Ca/Fe	Xpx Mn/Fe	STE Fo wt%	STE Al ppm	STE Fe ppm	STE Mn ppm	STE Mg ppm	STE Ca ppm	STE Ni ppm	STE Co ppm	STE Cr ppm
WPM-THICK	OIB	(S38)	953C-93R-06 45-55	Atlantic Ocean	Gran Canaria	4	82.31	167	128922	1748	261052	1930	2485	187	219	1.356	0.952	1.227	1.497	0.674	0.20	12	1377	18	908	61	74	5	6
WPM-THICK	OIB	(S38)	953C-93R-4 18-24	Atlantic Ocean	Gran Canaria	5	87.75	181	91591	1300	285495	1602	3239	168	416	1.419	1.135	1.039	1.749	0.544	0.18	13	1284	16	702	53	180	3	26
KOMATIITES	KOMATIITES	(S39)	MUN-24	Canada	Munro 2.7 Ga	65	92.34	392	58523	925	307010	1562	3316		1441	1.580	1.080	0.632	2.669	0.210	0.03	4	223	4	182	4	4		6
KOMATIITES	KOMATIITES	(S39)	MUN-414	Canada	Munro 2.7 Ga	63	89.42	254	80218	1238	294887	1625	2942		732	1.543	0.998	0.800	2.026	0.288	0.03	3	205	4	166	5	5		8
KOMATIITES	KOMATIITES	(S39)	Ch-11a	Canada	Munro 2.7 Ga	32	88.82	299	84803	1339	293033	1645	3034		791	1.579	1.035	0.878	1.940	0.212	0.04	5	327	7	214	8	6		16
KOMATIITES	KOMATIITES	(S40)	M-626	Canada	Alexo 2.7 Ga	11	92.81	334	55132	862	309510	1490	3461		1299	1.564	1.118	0.617	2.703	0.243	0.10	7	772	13	474	7	10		20
KOMATIITES	KOMATIITES	(S40)	M-767	Canada	Alexo 2.7 Ga	8	93.53	390	49829	801	313247	1484	3481		1308	1.607	1.111	0.554	2.978	0.155	0.14	14	1082	13	575	10	41		30
KOMATIITES	KOMATIITES	(S40)	M-666	Canada	Alexo 2.7 Ga	33	94.30	421	43881	719	315979	1484	3353		1263	1.638	1.061	0.466	3.381	0.091	0.05	9	404	5	274	5	6		20
KOMATIITES	KOMATIITES	(S41)	MZ-4	Zimbabwe	Belingwe 2.7 Ga	9	92.60	361	56373	885	307189	1494	3630	128	1327	1.571	1.182	0.666	2.651	0.230	0.11	10	796	13	477	6	8	2	32
KOMATIITES	KOMATIITES	(S42)	G-21	Canada	Gilmour 1.9 Ga	15	92.03	359	60841	948	305902	1762	3351		1058	1.558	1.095	0.667	2.897	0.256	0.08	8	626	9	327	11	18		25
KOMATIITES	KOMATIITES	(S42)	G-18	Canada	Gilmour 1.9 Ga	2	91.83	352	62561	968	305804	1787	3304		1071	1.547	1.080	0.676	2.856	0.278	0.36	3	2662	46	1468	14	35		38
KOMATIITES	KOMATIITES	(S42)	G-15	Canada	Gilmour 1.9 Ga	63	88.74	222	85277	1281	292437	1796	2190		652	1.503	0.749	0.639	2.106	0.371	0.04	3	263	4	156	2	3		5
KOMATIITES	KOMATIITES	(S42)	G-8a	Canada	Gilmour 1.9 Ga	70	88.67	244	85637	1284	291770	1793	2617		675	1.500	0.897	0.768	2.094	0.377	0.03	6	209	3	124	3	5		9
KOMATIITES	KOMATIITES	(S43)	GOR-94-19	Gorgona	Gorgona 0.9 Ga	71	91.44	549	64607	1051	300452	2140	3593		920	1.626	1.196	0.773	3.313	0.115	0.02	4	126	2	117	2	5		5
KOMATIITES	KOMATIITES	(S43)	GOR94-35	Gorgona	Gorgona 0.9 Ga	13	92.58	533	56770	930	308331	2120	3447		1167	1.638	1.118	0.635	3.734	0.090	0.08	10	613	11	396	10	16		41
KOMATIITES	KOMATIITES	(S43)	GOR94-34	Gorgona	Gorgona 0.9 Ga	27	91.50	473	64764	1042	303202	2274	3247		1003	1.609	1.071	0.694	3.511	0.150	0.05	12	402	7	256	12	12		15
KOMATIITES	KOMATIITES	(S43)	GOR94-32	Gorgona	Gorgona 0.9 Ga	18	92.79	544	54632	907	305920	2121	3482		1195	1.661	1.138	0.622	3.882	0.043	0.07	18	527	9	266	12	10		29

Notes for Table S2a. Concentrations and standard errors of mean (STE) are shown for elements in ppm and for Fo in mol%.
N-number of averaged high-Mg olivines (see text for definition). Samples marked (i) and (ii) represent different compositional groups of olivine within the same sample. Samples marked (n) represent an additional independent population of olivines analyzed for the same sample. References include samples description, unpb- unpublished. *- Ontong Java Plateau samples were arbitrary classified as WPM-THICK, but actually may belong to WPM-THIN at the time of formation.

News

We hope that you enjoy this section of Earth Pages. It gives one geologist's personal views about some of the major stories that appeared in leading journals, such as Geology, Science and Nature, in the last month. The items have been written and compiled by Steve Drury author of a number of Earth science books, including *Stepping Stones: The Making of our Home World* (Oxford University Press, 1999) and *Image Interpretation in Geology (3rd edition)* (Taylor & Francis, and Blackwell Science (USA), 2001).

If you have comments on this month's items you can contact the author at s.a.drury@open.ac.uk

• News Archive

News for May 2007

- Anthropology and geoarchaeology
- Climate change and palaeoclimatology
- Geobiology, palaeontology, and evolution
- Geochemistry, mineralogy, petrology and volcanology
- Planetary, extraterrestrial geology, and meteoritics
- Tectonics

Magmas from the mantle and recycled crust

May 2007

Two processes result in the Earth's mantle consuming rocks that formed oceanic and continental crust: subduction of oceanic lithosphere, and delamination from the base of thickened continental crust. In both cases the rocks involved are likely to be dominantly basaltic in composition. Those from the continental crust probably include mafic layered complexes, representing magma chambers in which intermediate magmas had resulted from fractional crystallization of basalt magma, and undifferentiated mafic igneous rocks underplated to the crust. Highly fractionated materials from the upper continental crust may also make their way into the mantle in the sedimentary cover to subducted ocean-floor basaltic crust.

New magmas originate in various ways as partial melts of ultramafic mantle rocks. Yet 4 billion years worth or more of consumed masses of crustal rocks must increasingly become involved in the chemistry of mantle melting by adding to its heterogeneity. Mantle heterogeneity is well-established from several lines of evidence provided by isotopic and trace-element analyses of modern basaltic lavas erupted in different tectonic settings. Yet, judging the influence and role of recycled crust have so far been plagued by data that are ambiguous. One outcome of previous research is that some ocean island basalt magmas formed by partial melting of peridotite whose chemistry had been transformed previously by other melts that had flowed through it (see Herzberg, C. 2007. Food for a volcanic diet. *Science*, v. **316**, p. 378-379).

A large team of geochemists, combining forces (and their data) from Russia, Germany, Australia, France, Taiwan, Eritrea, Britain, the USA, the Netherlands and Iceland, have sought to reduce the ambiguities by focussing on the chemistry of olivine phenocrysts found in basaltic lavas, rather than that of whole-rock samples (Sobolev, A.V. and 19 others 2007. The amount of recycled crust in sources of mantle-derived melts. *Science*, v. **316**, p. 412-417). Dominantly basaltic crustal masses in the mantle would melt to form silica-rich magmas. Passing through mantle peridotite, such melts would transform parts of the mantle to olivine-free pyroxenite. Magmas derived by partial melting of pyroxenite in the upper mantle would be basaltic, but enriched in silicon and nickel, and depleted in magnesium, calcium and manganese partly retained in the residual pyroxenes. Olivines crystallising first from basalt magmas carry a chemical signature of the parental melt composition, and thus the source.

The olivine approach by Sobolev and colleagues provides evidence for recycled crust in products of all kinds of basaltic magmatism, ranging from a contribution of 5% in ocean-floor basalts formed at ridges to about 20% in within-plate basalts. The contribution of mantle transformed to pyroxenite by chemical interaction with melt from foundered crustal masses ranges from 10% in mid-ocean ridge basalts to 100% in within-plate basalts formed below thick continental lithosphere. These include the largest volcanic outpourings in Earth's history, in the form of continental flood basalts. The largest of these, the Siberian Traps, accompanied the largest mass extinction of the Phanerozoic at the end of the Permian Period.
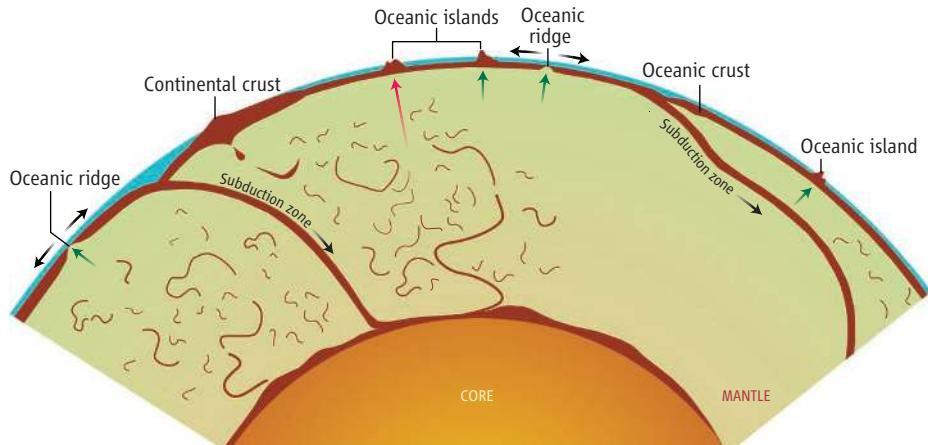
GEOCHEMISTRY

Food for a Volcanic Diet

Chemical analyses of lava can now reveal the nature of the rocks deep in the Earth that melted and rose to generate specific volcanoes.

Claude Herzberg

Volcanic eruptions have the power to reshape Earth's landscape, alter climate, and affect life. To understand how this works requires that we go deep into the Earth to learn exactly what kind of rock melts to produce magmas and the chemistry of this source rock. These are fundamental problems in geology, and they are also among the most difficult to understand. On page 412 in this issue, Sobolev *et al.* (*1*) describe a method for identifying some of these source rocks. We can think of them as food for volcanoes in the sense that they melt to provide the magmas that can erupt to the surface. To understand what Sobolev *et al.* have done and the ramifications that go beyond Earth science, we need to start with a refresher in geology.

Earth's mantle consists mostly of peridotite, a rock rich in the mineral olivine $(Mg,Fe)_2SiO_4$. When peridotite partially melts, the liquids collect to magmas that rise to the crust, give off gases like SO_2, CO_2, and H_2O, and solidify to basalt, a rock rich in the minerals clinopyroxene $[Ca(Mg,Fe)Si_2O_6]$ and plagioclase $[(Ca,Na)(Al_{1-2}Si_{2-3})O_8]$. Portions of these outer layers can be recycled back into the mantle at subduction zones and below thickened continents (see the figure). The recycled basaltic crust is transformed to a new rock called pyroxenite, so-called because it is rich in clinopyroxene. It may pile up on Earth's core, or be mixed back into the mantle with structures that have

The author is in the Department of Geological Sciences, Rutgers University, Piscataway, NJ 08854, USA. E-mail: herzberg@rci.rutgers.edu

Models of Earth's crust and mantle. Oceanic crust (brown) is solidified liquid that forms by partial melting of mantle peridotite (green) at oceanic ridges; together with sediment, oceanic crust can be recycled back into the mantle at subduction zones (*2*, *3*, *6*). Continental crust (brown) forms at subduction zones and can be recycled when it thickens by delamination (*5*, *15*). All crust (brown) is transformed to pyroxenite (brown) when recycled. Green arrow denotes melting peridotite. Red arrow denotes melting pyroxenite. Recycled crust may be distributed uniformly throughout the mantle, or it may be concentrated in certain hemispheres or depths. Crustal thickness is exaggerated for clarity, but ranges from ~6 to 40 km at the present time. Recycling is expected to reduce crust to dimensions ranging from micrometers to kilometers.

been described as marble cake (*2*), plum pudding (*3*), spaghetti (*4*), and gumbo (*5*) (see the figure). Volcanoes like those of Hawaii can melt from source rocks consisting of peridotite and/or pyroxenite from recycled crust. Sobolev *et al.* describe a method for identifying this rock based on the chemistry of lavas on volcanoes.

Sobolev *et al.* determined that many volcanoes melted from recycled crust, a conclusion that is not new (*6*). However, there has always been some ambiguity with past methods of identifying recycled crust based on the isotope

and trace-element geochemistry of lavas at the surface. New interpretations suggest that many oceanic islands melted from mantle peridotite that had been modified by melts that flowed through it (*7*, *8*), a process called metasomatism (*9*). Because it makes no difference to an atom of lanthanum, for example, whether it ends up concentrated in the crust or as metasomatized peridotite, using it as a tracer can be ambiguous and nonunique (*7*, *8*).

A breakthrough came when Sobolev *et al.* (*10*) showed that the nickel contents of many

olivine crystals in Hawaiian lavas were higher than those expected from melts of peridotite, and they preferred to explain this with a recycled crust source instead. But a lingering ambiguity is that a high nickel content in olivine can also arise when peridotite is enriched in pyroxene by melt-rock reaction (*11*). Supporting evidence for the recycled-crust interpretation (*10*) comes from the calcium contents of the Hawaiian lavas, which are too low to be easily explained by melting peridotite (*12*). Nickel and calcium are therefore telling the same story. That is, the main shield-building lavas at Hawaii were melted from a pyroxenite source rock that required the involvement of recycled crust as proposed by Sobolev *et al*. (*10*). The authors go further in that they examine the problem that arises when nickel, calcium, and manganese are used, and they extend the analysis to a larger population of volcanoes. Their results, together with other recent studies (*7, 8, 11*), show that it is unlikely that a single rock type will be an appropriate source for all oceanic volcanoes. For example, recycled crust is an important source rock for the Hawaiian islands (*1, 10, 12*), whereas metasomatized peridotite is the source rock for the Cook islands (*7*). An outstanding question is whether peridotite sources become metasomatized by melted recycled crust (*13*) or in some other way (*7, 8*).

Future studies might allow us to transform our picture from hypothetical models to actual three-dimensional views showing the size and distribution of recycled crust in the mantle. The implications go far beyond geology. For example, it may be no surprise that Sobolev *et al*. (*1*) identify pyroxenite as the rock that melted to produce the Siberian Traps. This was a magmatic flood on land so massive in scale that it triggered the largest mass extinction of life on Earth, some 250 million years ago (*14*). Although the exact causal links remain poorly understood in detail, one can reasonably imagine a different outcome if the mantle diet had less pyroxenite and more peridotite. Under these circumstances, less magma would have been produced and made available for eruptive flooding, and Earth's biosphere could have evolved along different pathways.

References

1. A. V. Sobolev *et al.*, *Science*, **316**, 412 (2007); published online 29 March 2007 (10.1126/science.1138113).
2. C. J. Allègre, D. L. Turcotte, *Nature* **323**, 123 (1986).
3. J. P. Morgan, W. J. Morgan, *Earth Planet. Sci. Lett*. **170**, 215 (1999).
4. W. Abouchami *et al.*, *Nature* **434**, 851 (2005).
5. D. L. Anderson, *New Theory of the Earth* (Cambridge Univ. Press, Cambridge, ed. 2, 2007).
6. A. W. Hofmann, W. M. White, *Earth Planet. Sci. Lett*. **57**, 421 (1982).
7. S. Pilet *et al., Earth Planet. Sci. Lett*. **236**, 148 (2005).
8. Y. Niu, M. J. O'Hara, *J. Geophys. Res*. **108**, 2209 (2003).
9. J.-L. Bodinier *et al.*, *J. Petrol*. **45**, 1 (2004).
10. A. V. Sobolev *et al.*, *Nature* **434**, 590 (2005).
11. P. B. Kelemen *et al.*, *Earth Planet. Sci. Lett*. **164**, 387 (1998).
12. C. Herzberg, *Nature* **444**, 605 (2006).
13. R. Dasgupta *et al.*, *J. Petrol*. **47**, 647 (2006).
14. I. H. Campbell *et al.*, *Science* **258**, 1760 (1992).
15. C. Herzberg *et al.*, *Contrib. Mineral. Petrol*. **84**, 1 (1983).